



Diurnally Modulated Cumulus Moistening in the Preonset Stage of the Madden–Julian Oscillation during DYNAMO*

JAMES H. RUPPERT JR. AND RICHARD H. JOHNSON

Department of Atmospheric Science, Colorado State University, Fort Collins, Colorado

(Manuscript received 28 July 2014, in final form 28 November 2014)

ABSTRACT

Atmospheric soundings, radar, and air–sea flux measurements collected during Dynamics of the Madden–Julian Oscillation (DYNAMO) are employed to study MJO convective onset (i.e., the transition from shallow to deep convection) in the tropical Indian Ocean. The findings indicate that moistening of the low–midtroposphere during the preonset stage of the MJO is achieved by simultaneous changes in the convective cloud population and large-scale circulation. Namely, cumuliform clouds deepen and grow in areal coverage as the drying by large-scale subsidence and horizontal (westerly) advection wane. The reduction of large-scale subsidence is tied to the reduction of column radiative cooling during the preonset stage, which ultimately links back to the evolving cloud population. While net column moistening in the preonset stage is tied to large-scale circulation changes, a new finding of this study is the high degree to which the locally driven diurnal cycle invigorates convective clouds and cumulus moistening each day. This diurnal cycle is manifest in a daytime growth of cumulus clouds (in both depth and areal coverage) in response to oceanic diurnal warm layers, which drive a daytime increase of the air–sea fluxes of heat and moisture. This diurnally modulated convective cloud field exhibits prominent mesoscale organization in the form of open cells and horizontal convective rolls. It is hypothesized that the diurnal cycle and mesoscale cloud organization characteristic of the preonset stage of the MJO represent two manners in which local processes promote more vigorous daily-mean column moistening than would otherwise occur.

1. Introduction

The Madden–Julian oscillation (MJO; Madden and Julian 1971, 1972) dominates tropical intraseasonal (20–90 day) variability and influences global weather (e.g., tropical cyclone frequency, monsoon onset and variability, ENSO, and midlatitude storm tracks) through myriad tropical–extratropical teleconnections (Zhang 2005, 2013). Through these teleconnections the MJO acts as a “bridge” between weather and climate (Zhang 2013), thereby holding a critical key to our advancement beyond medium-range predictability (Hendon et al.

2000; Waliser et al. 2003, 2012; Lin et al. 2006; Moncrieff et al. 2012). While studies have elucidated the principal diabatic heating structure and convective cloud evolution of the MJO, the physics governing the transition from predominant shallow cumuli to widespread, organized deep convection during MJO convective initiation remains largely unsolved (Bladé and Hartmann 1993; Maloney and Hartmann 1998; Johnson et al. 1999; Stephens et al. 2004; Majda and Stechmann 2009; Jiang et al. 2011; Hohenegger and Stevens 2013; Zhang et al. 2013).

Investigating MJO convective initiation was a central objective of the Dynamics of the Madden–Julian Oscillation (DYNAMO) field campaign, which was conducted in the tropical Indian Ocean during 2011/12 boreal fall–winter in collaboration with Cooperative Indian Ocean Experiment on Intraseasonal Variability in the Year 2011 (CINDY), ARM MJO Investigation Experiment (AMIE), and Littoral Air–Sea Processes (LASP) (Yoneyama et al. 2013; Zhang et al. 2013). Herein, these efforts will be referred to collectively as

* Supplemental information related to this paper is available at the Journals Online website: <http://dx.doi.org/10.1175/JAS-D-14-0218.s1>.

Corresponding author address: James H. Ruppert Jr., Department of Atmospheric Science, Colorado State University, 1371 Campus Delivery, Fort Collins, CO 80523.
E-mail: ruppert@atmos.colostate.edu

DYNAMO. Two MJO events were comprehensively sampled in DYNAMO, providing an unprecedented opportunity to diagnose the key processes during the transition from shallow to deep convection in the MJO.

The MJO is a zonal overturning circulation that propagates eastward across the tropics at $\sim 5 \text{ m s}^{-1}$ in connection with an upper-level divergent wind pattern, which typically spans the global tropics (Madden and Julian 1972). The active phase is characterized by upper-level divergence and enhanced deep convection and the suppressed phase by upper-level convergence and mostly nonprecipitating shallow cumuli (Zhang 2005 and references therein). While the associated upper-level divergent wind signal can circumnavigate the globe several times (Matthews 2008; Gottschalck et al. 2013), convective coupling typically initiates (referred to as MJO initiation herein) in the Indian Ocean and ceases in the central Pacific Ocean (Madden and Julian 1972; Hendon and Salby 1994; Wheeler and Hendon 2004).

During the transition from suppressed to active conditions in the MJO (from an Eulerian viewpoint), the prevailing character of convective clouds evolves from shallow cumulus, to congestus, to deep cumulonimbus as the free troposphere transitions from dry, to moist up to midlevels, to fully moistened, respectively (DeMott and Rutledge 1998; Johnson et al. 1999; Kikuchi and Takayabu 2004; Benedict and Randall 2007; Haertel et al. 2008; Yoneyama et al. 2008; Riley et al. 2011; Del Genio et al. 2012). This well-documented coupling between moist convection and column humidity within the MJO fundamentally owes to the effects of entrainment on ascending moist-convective clouds. The entrainment of low relative-humidity air reduces the buoyancy of these clouds—thereby limiting their terminal height—while entrainment in moister conditions has less of a negative impact on their buoyancy (Austin 1948; Wei et al. 1998; Redelsperger et al. 2002; Derbyshire et al. 2004; Takemi et al. 2004; Waite and Khouider 2010).

The systematic deepening of convective clouds prior to the active phase has led many to argue that the free-tropospheric moistening by the antecedent populations of cumulus and congestus clouds is important for preconditioning the environment for subsequent deep convection (Johnson et al. 1999; Kemball-Cook and Weare 2001; Kikuchi and Takayabu 2004; Benedict and Randall 2007; Yoneyama et al. 2008; Waite and Khouider 2010). The concept of cumulus preconditioning, in the context of the MJO, originates from “discharge–recharge” theory (Hendon and Liebmann 1990; Rui and Wang 1990; Bladé and Hartmann 1993). While the implicit meaning of cumulus preconditioning has evolved over time, a flaw in the original concept is that cumulus cloud populations do not typically moisten (i.e., humidify) the troposphere

over a large scale independent of changes in large-scale circulation (Hohenegger and Stevens 2013).

Rather, large-scale circulation and humidity are intimately linked—that is, on the spatiotemporal scales important to the MJO, wherein temperature variations are relatively small (Charney 1963; Raymond 2001; Sobel et al. 2001). By this thinking, it is the feedbacks between convective clouds and large-scale circulation that are important rather than the activity of the convective cloud population alone. For instance, while large-scale subsidence and horizontal moisture advection, exert control over column humidity, and therefore over moist convection, clouds can reduce column radiative cooling. This reduction can in turn reduce large-scale subsidence (e.g., Mapes 2001), assuming negligible temperature variations, thereby providing a link between clouds and the large-scale column moisture source (Chikira 2014). Local processes that augment moist convection (e.g., mesoscale organized cloud systems and cold pools) can therefore communicate with the large-scale moisture source through such feedbacks.

One such process diagnosed in this study is the locally driven diurnal cycle. While net (i.e., daily mean) column humidity changes are linked to the slowly evolving large-scale circulation, the more rapid effects of diurnal variability can dominate temporal column humidity variations, as will be demonstrated herein for the periods of low–midlevel moistening prior to MJO convective onset in DYNAMO. During this preonset stage of the MJO, the diurnal cycle is manifest in a pronounced daytime invigoration of convective clouds and cumulus moistening of the low–midtroposphere, fundamentally driven by oceanic diurnal warm layers. This study employs several in situ observational datasets from DYNAMO, which are described in section 2. An overview of the two MJO events sampled in DYNAMO is provided in section 3 for large-scale context, wherein the periods of focus for the diurnal cycle analysis (section 4) are defined. Section 5 provides a summary of the study’s findings along with a discussion of the resulting implications.

2. Data and methods

The primary DYNAMO observations employed in this study—those from a sounding network, a cloud-sensitive radar, and an air–sea flux site—are available from http://data.eol.ucar.edu/master_list/?project=DYNAMO.

a. Gridded sounding analysis

The Indian Ocean sounding network was composed of six sites, making two quadrilaterals straddling the

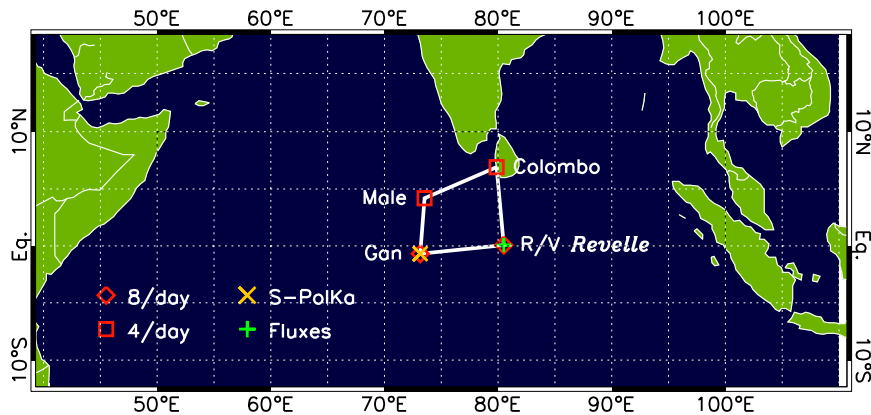


FIG. 1. DYNAMO northern sounding array for the period October–December 2011. Soundings were launched four to eight times per day, as indicated. Locations of the NCAR S-PolKa radar (Addu Atoll) and air–sea flux site (R/V *Revelle*) are also indicated.

equator, ~ 500 – 800 km on a side. The signals of the two (October and November) MJO events analyzed herein were well sampled by the northern quadrilateral, while the southern quadrilateral sampled intermittent deep convection connected to the intertropical convergence zone (ITCZ) (Johnson and Ciesielski 2013). This study is therefore limited to the northern quadrilateral (Fig. 1). This quadrilateral comprised three islands—Gan, Malé, and Colombo—and a ship—the R/V *Revelle*. Katsumata et al. (2011) demonstrate that a four-point quadrilateral array can accurately sample both the divergent and rotational flow components constituting the large-scale MJO circulation, while a triangular array does a poorer job. Therefore, periods when the R/V *Revelle* went offsite and the sounding array was reduced to three points are indicated in figures.

A comprehensive set of quality-control techniques has been applied to the DYNAMO soundings, including mitigation of the low-level heat island and flow blocking effects in the Colombo soundings due to the large island of Sri Lanka (Ciesielski et al. 2014a,b). Following quality control, the sounding observations were horizontally interpolated onto a 1° mesh using the multiquadric objective analysis technique of Nuss and Titley (1994) and vertically interpolated onto an isobaric grid at 25-hPa spacing from 1000 to 50 hPa. Several observational datasets were included in the interpolation to supplement the primary soundings (dropsondes, satellite-derived vector winds, scatterometer surface winds, and thermodynamic profiles from radio occultation measurements), the details of which are provided in a companion paper by Johnson et al. (2015). Vertical pressure velocity ω was calculated by vertically integrating divergence from the surface to the tropopause (with adiabatic flow assumed at the tropopause), with mass

balance applied using a constant divergence correction (O'Brien 1970). The gridded analysis was then spatially averaged over the northern sounding array to yield a time–pressure series of northern-array mean quantities.

During the special observing period (SOP: 1 October–15 December), soundings were launched eight (four) times per day at the equatorial (northern) sites (Fig. 1), though on 8 December launches at Colombo reduced to one time per day. Therefore, the analysis is carried out for 1 October–7 December. Temporal interpolation was carried out to generate data at 3-hourly frequency at the two northern sites (Fig. 1). This procedure was crucial for exploiting the 3-hourly information from the two equatorial sites, which resulted in markedly improved sampling of the diurnal cycle. The interpolation was performed for the analysis times of 0300, 0900, 1500, and 2100 UTC using the two soundings from 3 h prior to and following the given analysis time for the respective site (interpolation was not performed if either of these two soundings were missing). The error due to this procedure was assessed by exploiting the 3-hourly soundings at Gan. RMS differences between actual and contemporaneous Gan soundings generated by this procedure amounted to $\sim 0.5^\circ\text{C}$, 0.5 g kg^{-1} , and 1 m s^{-1} in temperature, specific humidity, and wind speed, respectively, which are inconsequential for the objectives of this study.

Similar analysis approaches to those described above have been successfully applied in many previous tropical and monsoon field campaigns [e.g., the Tropical Ocean Global Atmosphere Coupled Ocean–Atmosphere Response Experiment (COARE), the South China Sea Monsoon Experiment, the North American Monsoon Experiment, and the Terrain-influenced Monsoon

Rainfall Experiment], which have confirmed the reliability of results via comparison with independent observations (Lin and Johnson 1996a,b; Johnson and Ciesielski 2002; Ciesielski et al. 2003; Johnson et al. 2010; Ruppert et al. 2013). Detailed comparisons between the DYNAMO gridded sounding analysis and independent datasets are provided by Johnson et al. (2015) and are not repeated here. Provided in section 3, however, is a comparison between budget-derived and satellite-estimated rainfall.

b. Radar cloud measurements

The behavior of clouds is assessed using measurements from the National Center for Atmospheric Research (NCAR) dual-polarimetric and dual-frequency (10 cm: S band, and 8 mm: Ka band) S-PolKa weather research radar (Keeler et al. 2000), which was deployed during DYNAMO on Addu Atoll, Maldives, at 0.63°S, 73.10°E (to the northwest of Gan Island). (Only information from the S band is employed in this study.) The details of S-PolKa data quality-control and field-instrumentation management can be found at <https://www.eol.ucar.edu/instrumentation/remote-sensing/s-pol> and in prior studies (Powell and Houze 2013; Zuluaga and Houze 2013; Rowe and Houze 2014). When viewing S-PolKa data in this study, the caveat that the S-PolKa sampling region is far smaller than and on the corner of the northern sounding array must be considered. Slight inconsistencies in the timing between northern-array-averaged quantities and radar quantities are possible because of this issue.

Owing to its high sensitivity, the S-PolKa radar detects nonprecipitating clouds, which are important for moistening the troposphere to offset the drying by large-scale subsidence (Nitta and Esbensen 1974; Johnson and Lin 1997). This study employs the range–height indicator (RHI) echo measurements from the S-PolKa northeastern quadrant dataset, which is composed of vertical slices over azimuths from 4° to 82° (where there is minimal ground clutter) at 2° intervals, up to an elevation angle of 40°, and at 15-min sampling frequency. The maximum range of the RHI measurements is 150 km, though data are only retained within a 50-km range for this analysis, as advised by Feng et al. (2014). A subset of hydrometeor echo-base and echo-top height measurements is assembled from the dataset following interpolation of the data onto a Cartesian grid of 500-m vertical–horizontal spacing. Echo base and top are defined as the vertical boundaries of contiguous detectable echo return, with a minimum echo threshold of -30 dBZ (Feng et al. 2014). Then, echo features with a base elevation ≤ 1 km and vertical depth ≥ 1.5 km are isolated, thereby excluding very thin clouds and the

majority of Bragg scattering layers related to detrained moisture and turbulent mixing across vertical moisture gradients (Davison et al. 2013). Therefore, what are retained are boundary layer–based clouds and high-based clouds with contiguous detectable rain shafts. During suppressed periods, when rainfall is minimal and stratiform systems rare, these echo features are dominated by boundary layer–based convective clouds (Barnes and Houze 2013; Powell and Houze 2013; Zuluaga and Houze 2013; Rowe and Houze 2014).

Echo-top frequency is calculated from the above-described subset of echo features by counting the total occurrences of echo top at each vertical level as a function of time and normalizing this result by the total number of grid bins in the horizontal plane. Echo area coverage is calculated from the same subset by dividing the total number of horizontal grid points containing echo (at any level, subject to the above criteria) by the total number of grid points in the horizontal plane.

c. Auxiliary datasets

High-time-resolution (10 min) surface thermodynamic variables were collected during DYNAMO at the R/V *Revelle* (Fig. 1). The measurements employed herein include sea surface temperature (SST; following an adjustment to skin temperature), surface sensible and latent heat flux, wind speed, wind stress, and 10-m air temperature and humidity. Daily-mean latent heat flux from the TropFlux product (Praveen Kumar et al. 2012) is employed following an average over the northern sounding quadrilateral to facilitate the estimation of rainfall from the moisture budget. The Tropical Rainfall Measurement Mission (TRMM; Kummerow et al. 2000) 3B42v7 rainfall product (3-hourly frequency; Huffman et al. 2007) is employed, following an average over the northern sounding quadrilateral, for comparison with budget-derived rainfall. Orbit swath true-color images from Moderate Resolution Imaging Spectroradiometer (MODIS) are also employed, which were collected from <http://lance-modis.eosdis.nasa.gov/cgi-bin/imagery/realtime.cgi>.

3. Overview of the DYNAMO MJO events

Two MJO events were sampled by the DYNAMO northern sounding array during its full operation (October: MJO1; November: MJO2). The two MJO events are depicted in Fig. 2 as periods of very dry conditions [i.e., relative humidity (RH) $< 50\%$] through a deep layer with minimal rainfall, followed by very moist conditions (i.e., RH $> 70\%$) through most of the column with enhanced rainfall. These are the suppressed phase (MJO1: early–mid-October; MJO2: mid-November)

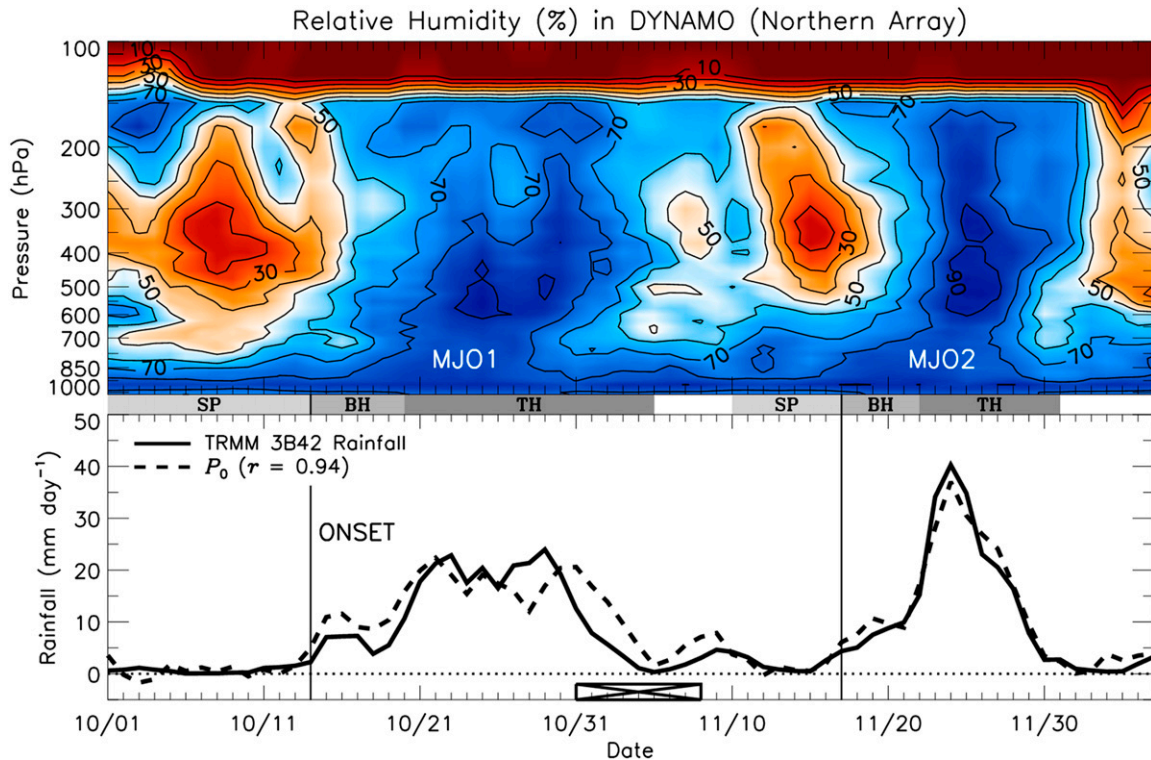


FIG. 2. (top) Time–pressure series of daily-mean relative humidity (RH; every 10%; with respect to ice where temperature $< 0^{\circ}\text{C}$) from the northern-array gridded analysis. (bottom) Daily-mean rainfall estimates (mm day^{-1}) from TRMM 3B42 (solid) and the moisture budget P_0 (dashed). All fields temporally smoothed using a 3-day running mean (smoothing in this and subsequent figures is applied using the “boxcar” technique). Correlation r between the smoothed rainfall estimates is indicated (significant at the 99% level). Here and in subsequent figures, “SP” refers to suppressed periods and “BH” (“TH”) refers to periods of bottom-heavy (top heavy) apparent heating, drying, and vertical motion profiles (Figs. 3 and 4), the black stretched-out \times along the lower abscissa indicates periods when the *Revelle* was on port call, and the vertical solid lines denote MJO onset (see text for definition).

and active phase (MJO1: late October–early November; MJO2: late November), respectively, which are separated by the vertical lines marking MJO onset in Fig. 2. (MJO onset, the MJO subperiods, and budget-derived rainfall P_0 , as depicted in Fig. 2, are explicitly defined later.) Dry conditions (i.e., $\text{RH} < 50\%$) reach down to ~ 800 hPa during the suppressed phase of MJO1, while dry conditions only reach ~ 550 hPa during that of MJO2. Differences in MJO event duration are also apparent, with both the suppressed and active phases of MJO1 outlasting those of MJO2 by roughly one week.

The bottom-up moistening that commences during the suppressed phase (Fig. 2) has been noted in numerous studies and likely relates to the deepening of convective clouds during this period (Lin and Johnson 1996a,b; Johnson et al. 1999; Kikuchi and Takayabu 2004; Kiladis et al. 2005; Benedict and Randall 2007; Haertel et al. 2008). The character of this low-to-midlevel moistening differs between MJO1 and MJO2, as described later. Moistening from aloft can also be

noted in Fig. 2 (e.g., ~ 15 – 20 November in the layer 150–300 hPa). Studies have related this moistening to the gravity wave or Kelvin wave response to the convective envelope of previous MJO events (Kiladis et al. 2001; Gottschalck et al. 2013; Johnson and Ciesielski 2013). Studies have also linked such gravity waves to the observed increase in cirrus clouds in the upper troposphere–lower stratosphere in the days–weeks prior to the MJO active phase, which can be observed as far as 30° east of the MJO convective envelope (Virts and Wallace 2010; Virts et al. 2010; Riley et al. 2011; Del Genio et al. 2012).

Figure 3 provides DYNAMO daily-averaged time–pressure series of the apparent heat source Q_1 and apparent moisture sink Q_2 , calculated according to Yanai et al. (1973):

$$\begin{aligned}
 Q_1 &\equiv \frac{D\bar{s}}{Dt} = \frac{\partial \bar{s}}{\partial t} + \bar{\mathbf{v}} \cdot \nabla \bar{s} + \bar{\omega} \frac{\partial \bar{s}}{\partial p} \\
 &= Q_R + L_v(\bar{c} - \bar{e}) - \frac{\partial}{\partial p}(\bar{\omega}'s') \quad \text{and} \quad (1)
 \end{aligned}$$

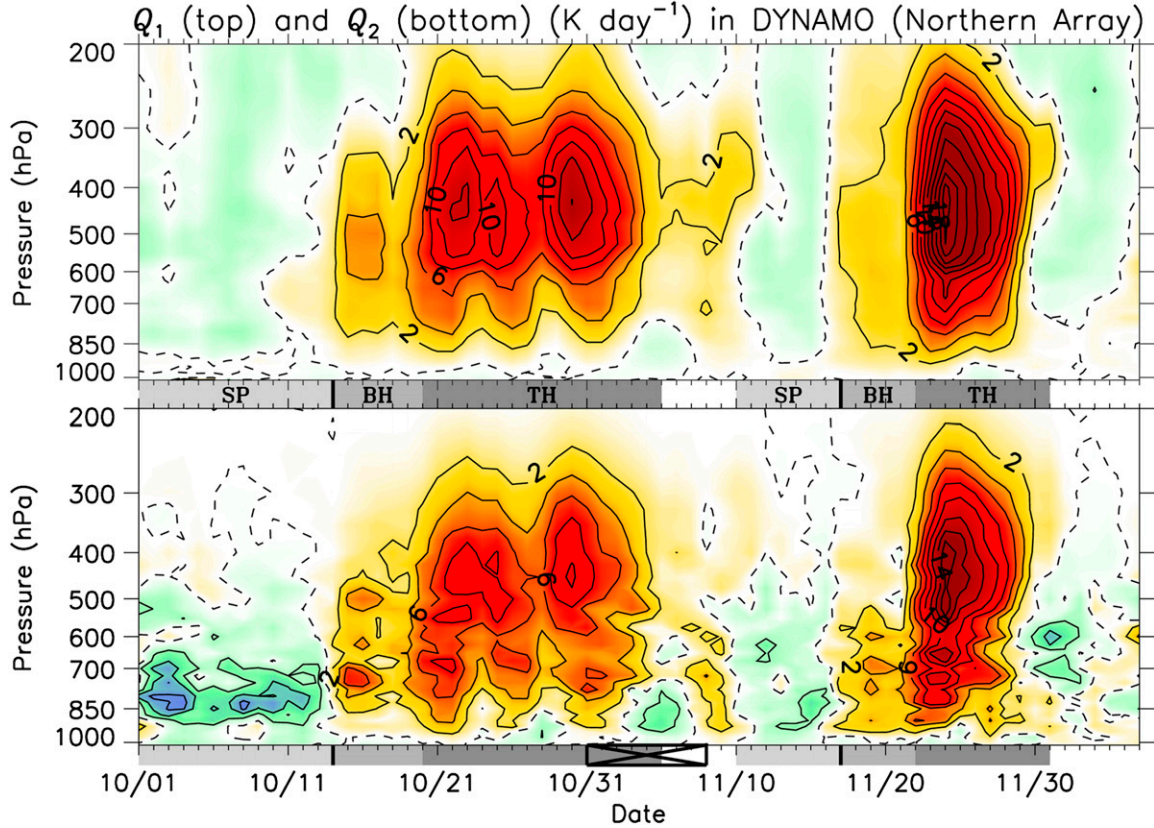


FIG. 3. Daily-mean time–pressure series of the (top) apparent heat source Q_1 and (bottom) apparent moisture sink Q_2 (contoured every 2 K day⁻¹ and shaded with positive values in red).¹ The zero contour is dashed. Three-day temporal smoothing applied.

$$\begin{aligned}
 Q_2 &\equiv -L_v \frac{D\bar{q}}{Dt} = -L_v \left(\frac{\partial \bar{q}}{\partial t} + \bar{\mathbf{v}} \cdot \nabla \bar{q} + \bar{\omega} \frac{\partial \bar{q}}{\partial p} \right) \\
 &= L_v (\bar{c} - \bar{e}) + L_v \frac{\partial}{\partial p} (\overline{\omega'q'}), \quad (2)
 \end{aligned}$$

with $s = c_p T + gz$ dry static energy, c_p the specific heat of dry air at constant pressure, T temperature, g gravity, z height, \mathbf{v} horizontal flow, ω vertical pressure velocity (Fig. 4), Q_R radiative heating, L_v the latent heat of vaporization at 0°C, $c(e)$ hydrometeor condensation (evaporation) rate, and q water vapor mixing ratio. Overbars denote a spatial average over the northern sounding array and primes deviations from that average. The heat and moisture source terms related to horizontal eddies and ice-phase processes do not appear in (1) and (2), although they can be included (Arakawa and Schubert 1974; Yanai and Johnson 1993). The LHSs of (1) and (2) are calculated directly from the gridded analysis.

MJO1 and MJO2 appear clearly in Fig. 3 and the time series of ω in Fig. 4. The quantities Q_1 and Q_2 are negative through most of the troposphere during the suppressed phases in connection with radiative cooling and moistening by clouds under subsidence, and Q_1 and Q_2 are positive during the two active phases, reflecting the large latent heating and drying due to precipitation with strong ascent. “MJO onset” refers to the time at which subsidence and apparent cooling and moistening switch to ascent and heating and drying (MJO1: 14 October; MJO2: 17 November; ascertained from unsmoothed, column-integrated fields), as indicated in the relevant figures. As Yanai et al. (1973) show, the vertically integrated budgets can be written as

$$\begin{aligned}
 \langle Q_1 \rangle &= \langle Q_R \rangle + \langle L_v (\bar{c} - \bar{e}) \rangle - \left\langle \frac{\partial}{\partial p} (\overline{\omega's'}) \right\rangle \\
 &= \langle Q_R \rangle + L_v P_0 + S_0 \quad \text{and} \quad (3)
 \end{aligned}$$

$$\begin{aligned}
 \langle Q_2 \rangle &= \langle L_v (\bar{c} - \bar{e}) \rangle + \left\langle L_v \frac{\partial}{\partial p} (\overline{\omega'q'}) \right\rangle \\
 &= L_v (P_0 - E_0), \quad (4)
 \end{aligned}$$

¹ Q_1 and Q_2 , as defined in (1) and (2), have been multiplied by the factor $(8.64 \times 10^4) c_p^{-1}$ for presentation in kelvins per day.

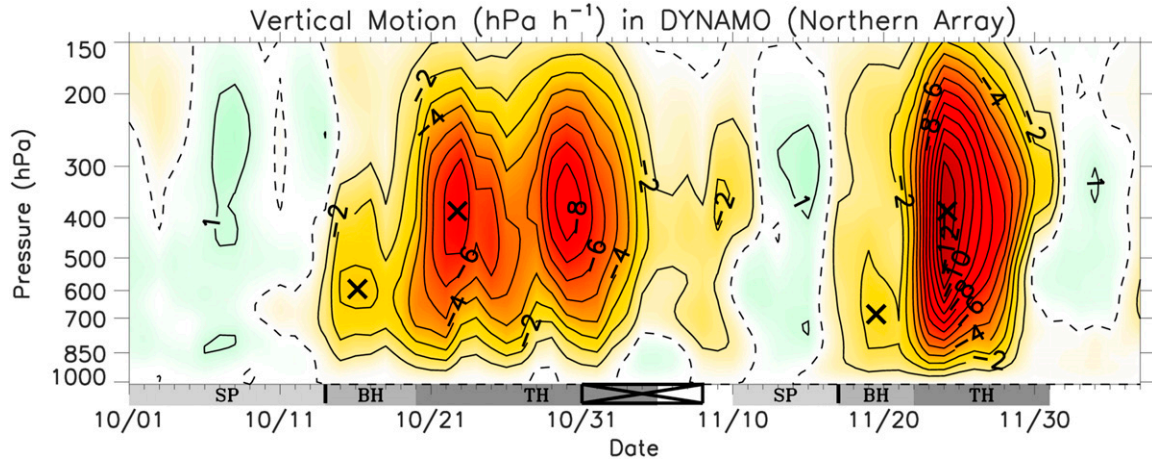


FIG. 4. As in Fig. 3, but for vertical pressure velocity ω (contoured every 2 hPa h^{-1} and shaded with negative values in red). The \times symbols are placed in several locations to highlight the level of maximum ascent.

where

$$\langle \cdot \rangle \equiv \frac{1}{g} \int_{p_T}^{p_{\text{sfc}}} (\cdot) dp,$$

P_0 is precipitation, S_0 is surface sensible heat flux, E_0 is surface evaporation rate, p_{sfc} is surface pressure, and p_T is 100 hPa (results insensitive to the choice of p_T). Precipitation P_0 , shown in Fig. 2, is calculated from (4) using E_0 from TropFlux averaged over the northern sounding array. Pearson's correlation coefficient r between TRMM rainfall and P_0 is 0.94 (significant at the 99% level using the Student's t test and assuming a sample size of 7, which is the approximate number of 10-day periods in the dataset). There are times when P_0 is slightly negative or departs measurably from TRMM rainfall, which could owe to any of several factors: observational sampling errors (Mapes et al. 2003), inaccuracies in E_0 from TropFlux, changes in cloud volume (which break the assumption that $P_0 = \langle \bar{c} - \bar{e} \rangle$; McNab and Betts 1978), or inaccuracies in TRMM rainfall (Liu et al. 2007). The marked agreement between P_0 and TRMM rainfall, however, lends confidence to the gridded sounding analysis and the moisture budget described next [see Johnson et al. (2015) for more detailed budget validation].

Presented next is the column-integrated water vapor budget (Fig. 5), which is employed in lieu of the column-integrated MSE budget (Sobel et al. 2014) since the latter hides the direct effects of clouds (i.e., the moistening–drying due to liquid–vapor phase changes). Furthermore, in the column-integrated MSE budget, vertical dry static energy advection typically cancels with moisture advection in the vertical advection term, therefore potentially hiding

the role of vertical advection. From (2) and (4), the column-integrated water vapor budget can be written as

$$\begin{aligned} \left\langle \frac{\partial L_v \bar{q}}{\partial t} \right\rangle &= -\langle \bar{\mathbf{v}} \cdot \nabla L_v \bar{q} \rangle - \left\langle \bar{\omega} \frac{\partial L_v \bar{q}}{\partial p} \right\rangle - \langle Q_2 \rangle \\ &= -\langle \bar{\mathbf{v}} \cdot \nabla L_v \bar{q} \rangle - \left\langle \bar{\omega} \frac{\partial L_v \bar{q}}{\partial p} \right\rangle + L_v (E_0 - P_0). \end{aligned} \quad (5)$$

According to (5), moistening and drying (in the Eulerian framework) are driven by horizontal and vertical advection (first and second RHS terms), as well as surface evaporation and precipitation (third and fourth RHS terms), or the apparent source and sink, respectively. Since, on the large scale, clear-air vertical motion is downward in the tropics (i.e., drying), moistening via vertical advection (i.e., ascending motion) in (5) should be regarded as the upward flux of moisture and evaporation of detrained hydrometeors by clouds, which in such cases dominate the sampled divergent circulation (e.g., Arakawa and Schubert 1974; Yanai et al. 1973; Chikira 2014). While the budget terms (as shown in Fig. 5) are smoothed, no means are removed; therefore, their individual contributions to column moistening are conveyed in the absolute sense.

Before discussing the individual terms in the moisture budget, three subdivisions of each MJO event are defined based on several key characteristics and transition points depicted in Figs. 2–4 (ascertained from unsmoothed fields). These subdivisions are depicted by shaded bars in all relevant figures. The suppressed phases (“SP”) are identified as the periods in which $\langle Q_2 \rangle < 0$ and subsidence prevails prior to MJO onset (1–13

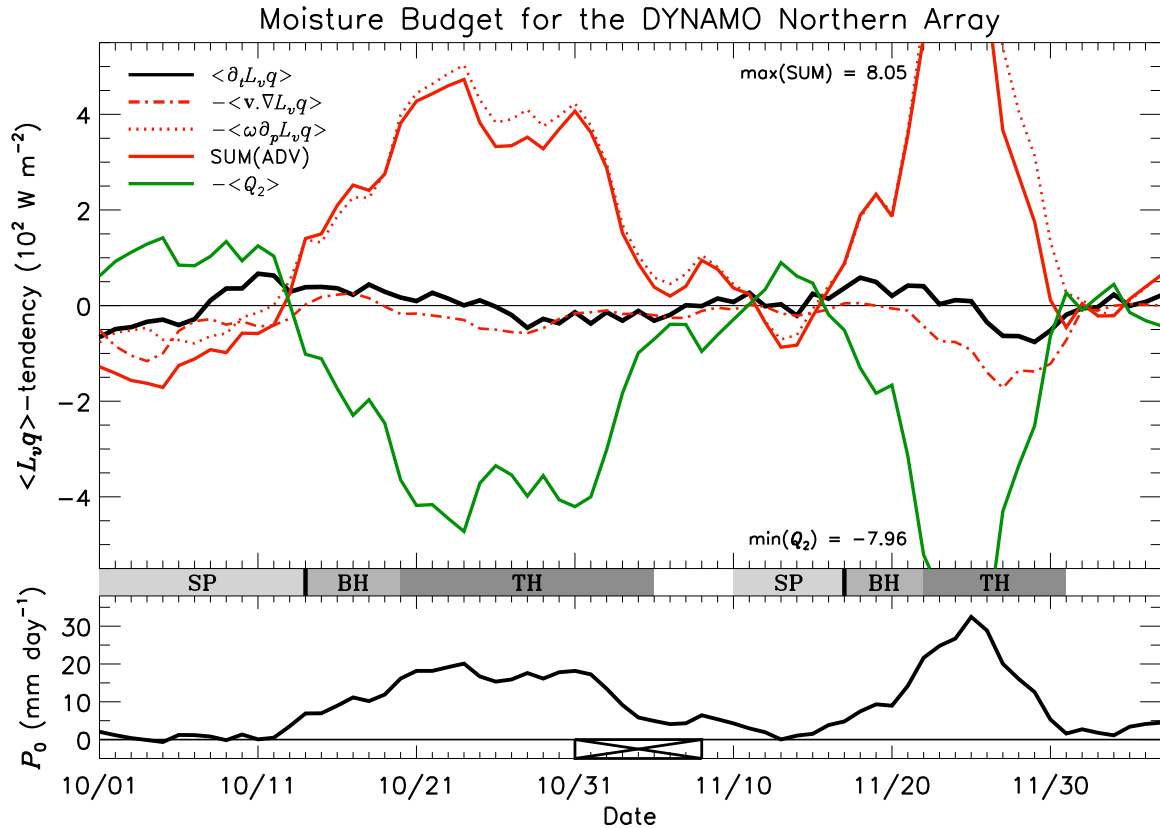


FIG. 5. (top) Daily-mean vertically integrated water vapor budget (10^2 W m^{-2}) and (bottom) budget rainfall P_0 (mm day^{-1}). Budget terms are calculated as shown in (5), with the Eulerian tendency (black), horizontal advection (red dotted-dashed), vertical advection (red dotted), the sum of horizontal and vertical advection [SUM(ADV); red solid], and apparent sources (green). Maximum and minimum values for terms exceeding the ordinate scale are indicated. Five-day temporal smoothing has been applied to all fields.

October and 10–16 November; end dates are inclusive). These periods are analogous to the preonset stage in DYNAMO parlance (Yoneyama et al. 2013). The active phases are split into two subperiods each. The first subperiods are those with relatively more bottom-heavy Q_1 , Q_2 , and ω profiles (“BH”; 14–19 October and 17–21 November), which correspond with positive moisture (i.e., $L_v q$) tendency (Fig. 5). The second are those characterized by top-heavy Q_1 , Q_2 , and ω profiles (“TH”), which exhibit progressively decreasing moisture tendency (20 October–4 November and 22–30 November).

The signs of Q_1 and Q_2 during SP (Fig. 3), together with the knowledge that $P_0 \sim 0$ (Fig. 2), imply specifically which heat and moisture sources/sinks are at play. From (3), the magnitude of $\langle Q_R \rangle$ must exceed that of S_0 , assuming $S_0 > 0$. From (4), the moistening signal in Q_2 owes primarily to $E_0 > 0$. Figure 5 reveals that this evaporative moistening works in opposition to the drying by subsidence and horizontal advection. These terms are $O(100 \text{ W m}^{-2})$ of moistening and drying, respectively. [Motivated by a reviewer comment, we have

confirmed that $L_v E_0$ calculated from TropFlux agrees very well with the magnitude of $-\langle Q_2 \rangle$ during SP in Fig. 5. This comparison is roughly equivalent to comparing TRMM rainfall and P_0 , as in Fig. 2, since P_0 is calculated using TropFlux in $\langle Q_2 \rangle / L_v + E_0$, from (4).] The quasi balance between large-scale drying and cumulus moistening is reminiscent of the tropical trade cumulus regimes described previously, though horizontal advection typically plays a smaller role in such regimes (Nitta and Esbensen 1974; Johnson and Lin 1997).

In SP–MJO1, the moisture tendency becomes positive around 7 October (Fig. 5). The low–midtropospheric moistening observed during the subsequent ~ 6 days (Fig. 2) is accomplished by surface evaporation (4), or alternatively, vertical eddy cloud transport (2), which overcomes the drying by large-scale circulation (Figs. 4 and 5). The waning of subsidence and horizontal-advective drying, while cumulus moistening persists, orchestrates the evolution of the moisture tendency, indicating the key role of large-scale circulation changes. In contrast to SP–MJO1, a period of moistening takes place early in SP–MJO2 [i.e., $\sim (850\text{--}550)$ hPa], followed

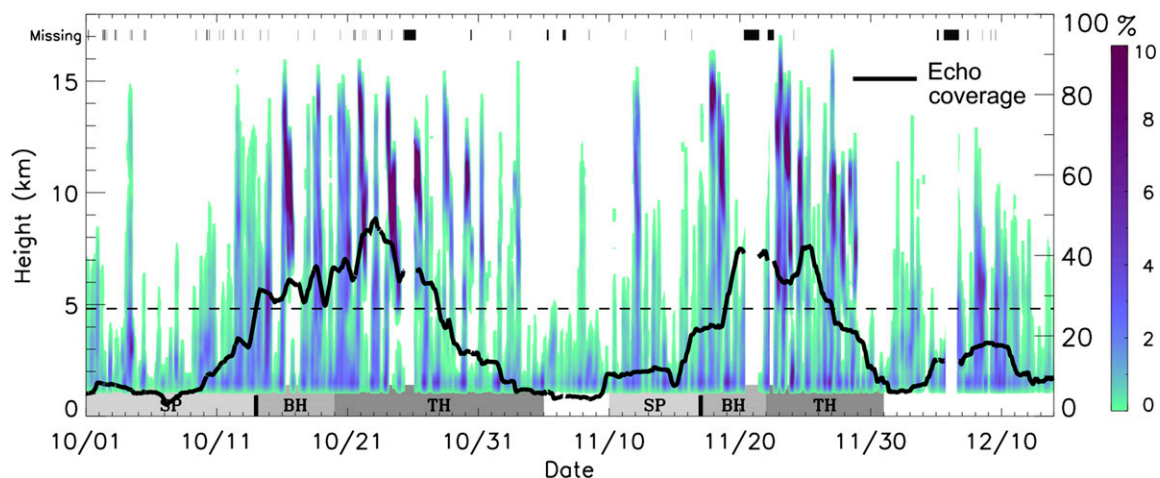


FIG. 6. Time–height series of echo-top frequency (shading; %) and echo area coverage (%; right axis) from 15-min S-PolKa RHI data (cf. section 2 for methodology). Temporal smoothing has been applied to echo-top frequency (echo area coverage) using a 6-h (5 day) running mean. Black hashes near the top indicate time periods of missing data (where the time gap between scans exceeded 23 min). The dashed line indicates the 0°C level.

by a persistent period of relatively moist conditions compared to SP–MJO1 (i.e., $RH \geq 50\%$ up to ~ 550 hPa), followed again by moistening beginning shortly before onset (Figs. 2 and 5). In spite of these differences between SP–MJO1 and SP–MJO2, the role of large-scale circulation is similar, in that column moistening is facilitated by the waning of large-scale drying (subsidence acts as the primary drying agent during SP–MJO2; Fig. 5).

At the time of onset in both MJOs, Q_2 switches to large drying because of rainfall as vertical advection switches to a large moisture source of $O(500 \text{ W m}^{-2})$ (Fig. 5). Horizontal advection is very weakly moistening in BH–MJO1. The moisture tendency remains positive during BH in both MJOs, reflecting the full-column moistening as depicted in Fig. 2. This second stage of moistening is accomplished in the presence of relatively bottom-heavy convection (Figs. 3 and 4), indicative of predominant congestus and cumulonimbus clouds. The relatively bottom-heavy heating implies that convective inflow (i.e., convergence) is focused over a relatively shallow depth of the lower troposphere, leading to a larger moisture source than a heating profile with a higher peak (i.e., as in stratiform precipitating systems) (Wu 2003; Zhang et al. 2004).

During TH, the moisture tendency becomes negative, aided by increased horizontal-advective drying. This drying likely reflects the dry-air intrusions associated with equatorward advection in Rossby gyres on the west side of the active phase (Gill 1980; Chen et al. 1996; Maloney and Hartmann 1998; Benedict and Randall 2007; Gottschalck et al. 2013; Kerns and Chen 2014).

Unsaturated downdrafts in stratiform precipitation systems also likely assist the drying (Figs. 3 and 4) (Zipser 1977; Barnes and Houze 2013; Zuluaga and Houze 2013; Chikira 2014; Rowe and Houze 2014). The end of each active phase is met with a return to conditions characteristic of SP.

A DYNAMO time series of echo-top frequency and echo area coverage (cf. section 2) is provided in Fig. 6. An abundance of short-time-scale variability is clear in echo-top frequency, particularly the 2-day modes during the active phase of MJO1, likely related to the westward-propagating 2-day waves described in past studies (Haertel et al. 2008; Johnson and Ciesielski 2013; Zuluaga and Houze 2013). There is also a clear, slower evolution of convection related to the MJO. Shallow cumulus and congestus clouds with tops < 10 km prevail during SP, with a progressive deepening of clouds prior to and around MJO onset. Clouds are generally deeper in SP–MJO2, consistent with a deeper moist layer (Fig. 2). Echo tops > 12 km prevail thereafter during the active phase. Echo area coverage increases from $\sim 10\%$ to $\sim 30\%$ during this transition, indicating that cloud systems are both deepening (in echo-top height) and increasing in abundance and/or size leading up to and shortly after MJO onset. Echo area coverage maximizes around 50% early in TH–MJO1, with dual peaks of $\sim 40\%$ in BH and TH–MJO2. Echo-area coverage (Fig. 6), diabatic heating (Fig. 3), column humidity (Figs. 2 and 5), and rainfall all exhibit close correspondence in both tendency and time of peak values. These findings are generally consistent with those of Xu and Rutledge (2014).

The findings of this section demonstrate that moistening of the troposphere in the MJO preonset stage is orchestrated by simultaneous changes in large-scale circulation and the convective cloud population. While there are differences between the suppressed phases of MJO1 and MJO2 (i.e., in the character and duration of moistening and depth of the moist layer; Fig. 2), the role of large-scale circulation is similar in both. Namely, moistening of the low–midtroposphere (Fig. 2) is accomplished by the waning of drying due to subsidence and horizontal advection (Figs. 4 and 5) as the population of convective clouds is simultaneously invigorated. Invigoration of the cloud population is manifest in a deepening and increase in the areal coverage of clouds (Fig. 6). Moistening of the full column takes place after MJO onset (BH) in connection with relatively bottom-heavy diabatic heating, suggesting abundant congestus and cumulonimbus clouds and minimal stratiform rainfall (Fig. 3). The magnitude of diabatic heating increases with time as column humidity and echo area coverage increase from BH into TH (though there is an earlier peak in echo coverage in BH–MJO2). Column drying begins during TH in connection with top-heavy diabatic heating and is assisted by increased horizontal dry-air advection. Rainfall approximately correlates with column humidity, therefore maximizing around the time that column moistening ceases (i.e., early in TH). This evolution is consistent with previous studies (Maloney and Hartmann 1998; Johnson et al. 1999; Benedict and Randall 2007; Del Genio et al. 2012; Barnes and Houze 2013; Johnson and Ciesielski 2013; Zuluaga and Houze 2013; Xu and Rutledge 2014).

Variations in both vertical and horizontal advection are important, which is consistent with the findings of Sobel et al. (2014). Horizontal advection, as depicted in Fig. 5, is largely manifest in a waxing and waning of drying related to enhanced (suppressed) equatorward dry-air advection due to Rossby wave activity during the late-active phase (preonset stage) (Gottschalck et al. 2013; Kerns and Chen 2014). Studies demonstrate that enhanced anomalous horizontal-advective drying (moistening) is associated with enhanced westerly (easterly) flow (Johnson and Ciesielski 2013; Kerns and Chen 2014; Sobel et al. 2014). The waning of subsidence during the preonset stage may be linked to both remote and local effects. Eastward-propagating gravity or Kelvin waves are likely important for decreasing upper-level convergence prior to onset (Kiladis et al. 2001; Virts and Wallace 2010; Virts et al. 2010; Gottschalck et al. 2013; Johnson and Ciesielski 2013). Observations also depict a reduction in outgoing longwave radiation during the

preonset phase (Johnson et al. 2015; Sobel et al. 2014). This reduction in column radiative cooling—likely driven by the local invigoration of moist convection (Fig. 6) and/or development of high cirrus clouds during the preonset stage (Virts and Wallace 2010; Virts et al. 2010)—must equate to reduced large-scale subsidence when temperature variations are assumed negligible (Mapes 2001; Chikira 2014).

Since the local invigoration of moist convection during the preonset stage is intimately linked with the coinciding humidification of the low–midtroposphere (Figs. 2, 5, and 6), a better understanding of the key physics in MJO onset may come from improved understanding of this convective invigoration. The next section of this study exploits the unique opportunity afforded by DYNAMO to describe the local influences on convective invigoration in MJO onset. The findings will demonstrate that moist convection exhibits a pronounced locally driven diurnal cycle, with cumulus invigoration occurring distinctly each afternoon in response to the formation of oceanic diurnal warm layers. This diurnal cycle drives a major component of Eulerian column humidity variations during the preonset stage.

4. The diurnal cycle of cumulus moistening

Time series of the column-integrated Eulerian moisture tendency (i.e., $\langle \partial \bar{q} / \partial t \rangle$) spanning the two MJO suppressed phases reveal the importance of short-time-scale variability during these periods (Fig. 7). There is a clear prominence of cyclic variability with period ≤ 24 h. Comparison between the unfiltered Eulerian tendency and the same term smoothed with a 24-h running mean (i.e., $\langle \partial \bar{q} / \partial t \rangle_{\text{DAILY}}$) confirms this point (Fig. 7). The variance of $\langle \partial \bar{q} / \partial t \rangle$ over the period 1 October–7 December is ~ 74 (mm day^{-1})², as compared with ~ 9 (mm day^{-1})² in $\langle \partial \bar{q} / \partial t \rangle_{\text{DAILY}}$; in other words, $\sim 90\%$ of the total variance of the Eulerian column moisture tendency is explained by diurnal and subdiurnal variability during these periods (this fraction exceeds 90% when the periods shown in Fig. 7 are isolated for the variance calculations). The diurnal cycle in the advective moisture source is negligible (not shown), corroborating that the diurnal cycle is primarily locally driven.

While there are differences between the two MJO events (e.g., greater semidiurnal variability in SP–MJO1), the diurnal cycle is clearly important, with moistening often peaking in the afternoon (Fig. 7). The relationships between independent datasets portray a coherent diurnal cycle in moist convection, as will be demonstrated. This diurnal cycle, with pronounced afternoon convection, implies the importance of daytime

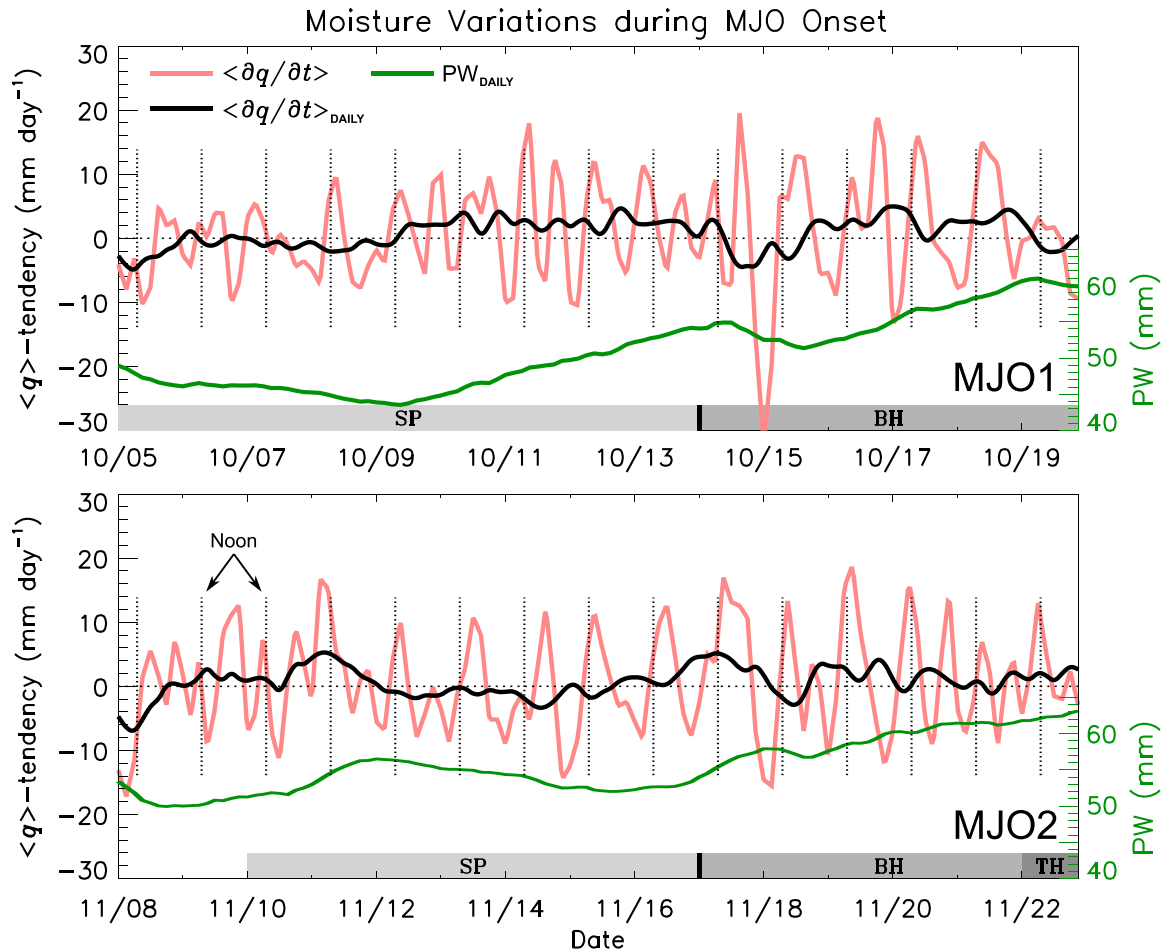


FIG. 7. Time series of the northern-array mean, column-integrated Eulerian moisture tendency (mm day^{-1} ; left axis) spanning convective onset in (top) MJO1 and (bottom) MJO2. The 3-hourly Eulerian tendency $\langle \partial q / \partial t \rangle$ is depicted (red), and $\langle \partial q / \partial t \rangle_{\text{DAILY}}$ (black) is the same except smoothed using a 24-h running mean. Precipitable water smoothed using a 24-h running mean (PW_{DAILY} ; green; mm; right axis) is also shown. The vertical lines denote local noon.

upper-ocean warming (Sui et al. 1997). In this sense, the diurnal cycle differs from that of more disturbed tropical oceanic regimes, wherein overnight convective activity dominates owing to enhanced oceanic mixing (i.e., prevention of large diurnal SST swings) and nocturnally maximized radiative cooling from the upper part of clouds (Gray and Jacobson 1977; Randall et al. 1991; Xu and Randall 1995; Chen and Houze 1997; Sui et al. 1998; Dai 2001; Yang and Smith 2006; Johnson 2011).

A time series of SST from the R/V *Revelle* during DYNAMO depicts a very prominent diurnal cycle (Fig. 8). The diurnal cycle is most regular and/or largest during the suppressed periods when $\text{SST}_{\text{daily}}$ (SST smoothed with a 24-h running mean) is climbing, with the greatest diurnal increase appearing on 16 November, from 29.3° to 32.1°C over the period 0650–1530 LT (L)—that is, a remarkable increase of

2.8°C in 9 h. Similar rapid warming was observed during light-wind periods in COARE (Weller and Anderson 1996). These large diurnal SST swings occur under clear, light-wind conditions owing to the formation of upper-ocean diurnal warm layers, whereby daytime heating stabilizes the upper ocean, inhibits vertical mixing, and hence concentrates subsequent solar heating to within this surface layer (Halpern and Reed 1976; Stramma et al. 1986; Flament et al. 1994; Webster et al. 1996; Weller and Anderson 1996; Kawai and Wada 2007; Bellenger et al. 2010; Matthews et al. 2014). Studies demonstrate that this diurnal cycle is key to rectifying the slower (i.e., daily mean) warming preceding MJO onset (Bernie et al. 2005; Matthews et al. 2014). Greater wind speeds limit the diurnal SST range by enhancing vertical mixing (e.g., compare SP–MJO1 with SP–MJO2; Fig. 8).

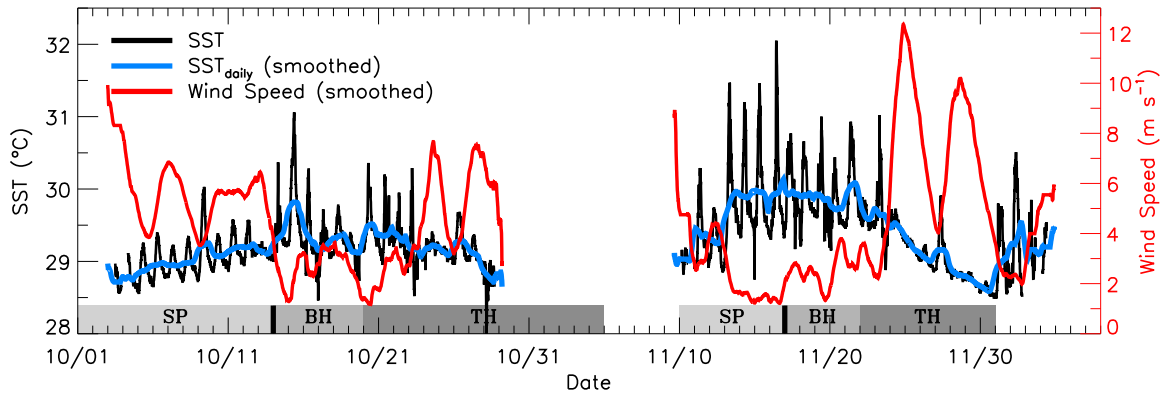


FIG. 8. Time series of 10-min-frequency SST (adjusted to skin temperature; black; °C; left axis), SST smoothed using a 24-h running mean (SST_{daily} ; blue), and surface wind speed smoothed using a 24-h running mean (red; m s^{-1} ; right axis) from the *Revelle* flux site (Fig. 1).

Time series of surface flux measurements from the R/V *Revelle* spanning SP–MJO1 (Fig. 9) and SP–MJO2 (Fig. 10) corroborate the prominence of the diurnal cycle during these periods. During SP–MJO1, sensible heat flux (S_0) and 10-m air temperature often exhibit diurnal cycles closely following that of SST, though wind speed and latent heat flux ($L_v E_0$) are dominated by longer-time-scale variability. During SP–MJO2, however, SST, air temperature, S_0 , $L_v E_0$, and wind speed all exhibit clear, coherent diurnal cycles in the 4 days leading up to MJO onset. The relationship between variables is more clearly depicted in Fig. 11, which shows anomaly diurnal composites over the strongly diurnally modulated days (MJO1: 6–11 October; MJO2: 13–16 November).² These composites are calculated by averaging the time series as a function of time of day and removing the composite mean (the calculations were also carried out by removing daily means first to subtract the lower-frequency variability, and the results were virtually identical; not shown). During the period in SP–MJO2, there is a composite-average night–day SST variation of $\sim 1.5^\circ\text{C}$, with a peak at $\sim 1300\text{L}$. Night–day variations in air temperature, S_0 , $L_v E_0$, and wind speed are $\sim 1^\circ\text{C}$, $\sim 10\text{ W m}^{-2}$, $\sim 80\text{ W m}^{-2}$, and $\sim 2\text{ m s}^{-1}$, respectively (Fig. 11b). The diurnal cycle in air temperature suggests that the boundary layer is progressively warmed by increasing SST, which is tied to a progressive increase in wind speed as the mixed layer deepens (Johnson et al. 2001). The sudden air

temperature drop of $\sim 0.6^\circ\text{C}$ around 1400 L indicates the effect of evaporatively generated cold pools, which in turn provides a strong, albeit brief, boost to air–sea fluxes (Fig. 11b). Note, however, that the magnitude of this sudden cooling owes largely to a single event on 15 November (Fig. 10). The composite evolution of SST and fluxes is qualitatively similar during the October period, though with more limited diurnal variations, likely owing to larger mean wind speed (Figs. 8 and 11a). The large-scale cloud response to the diurnal variation in air–sea fluxes, during both SP–MJO1 and SP–MJO2, however, was substantial (shown later).

To assess the character of clouds in the DYNAMO array during the MJO suppressed phases, sets of true-color images from the MODIS *Aqua* and *Terra* satellites are provided, with samples for SP–MJO1 (Fig. 12) and SP–MJO2 (Fig. 13). The *Aqua* and *Terra* satellite overpass sequence provides closely overlapping regional sampling each day, though with a 3-h gap between each satellite’s overpass, thereby sampling the evolution of the cloud scene (from the late morning to the early afternoon). Since the overpasses shift each day, however, the sampling regions also shift. The images shown have been cropped from their originals with preference for regions nearest to the northern sounding array and away from image edges where the cloud scene is distorted. The most prominent feature of these cloud scenes is the high degree of mesoscale organization—virtually all clouds are part of either cloud streets (Figs. 12b,c and 13h), indicative of horizontal convective rolls (HCRs; Weckwerth et al. 1996), or open cells (Figs. 12c–f and 13a,b,d–f). The open cells range in diameter from roughly 15 to 50 km. Open-cellular cloud organization was also noted in COARE (Johnson et al. 2001).

²Note that the selected date ranges for diurnal composites differ between some figures (i.e., Figs. 11, 14, 15, and 16). This is unavoidable when aiming to isolate diurnal variability and in datasets with differing sampling regions.

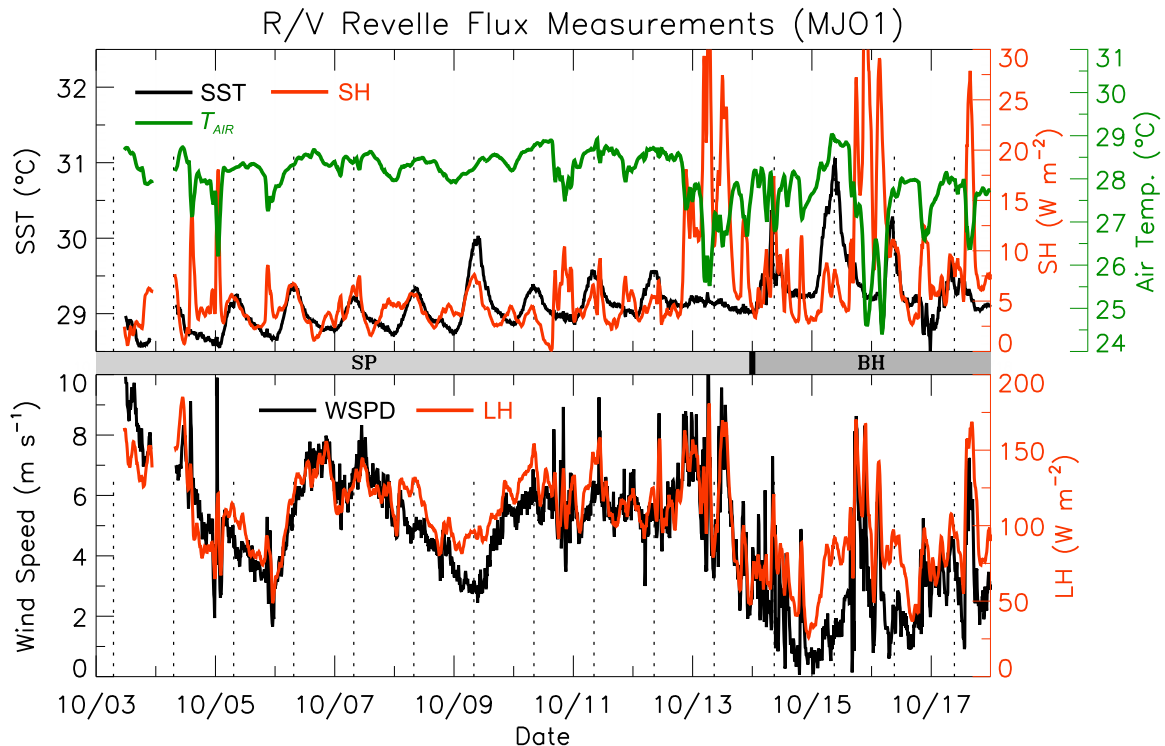


FIG. 9. (top) Time series spanning convective onset for MJO1 of SST (black; °C; left axis), 10-m air temperature (green; °C; outer-right axis), and surface sensible heat flux (SH; red; W m^{-2} ; inner-right axis) from the *Revelle*. (bottom) As in (top), but for wind speed (black; m s^{-1} ; left axis) and surface latent heat flux (LH; red; W m^{-2} ; right axis). SH and LH have been smoothed using a 1-h running mean. The vertical dotted lines indicate local noon.

While this organization fundamentally owes to heating from below by the warm ocean surface (i.e., Rayleigh–Bénard convection), the dimensionality of the organization relates to the dominance of shear-versus buoyancy-driven turbulence.

The mode of this organization can be estimated from the ratio z_i/L , where z_i is the depth of convective overturning, and L the Obukhov length, given by

$$L = -\frac{c_p \rho \theta_v u_*^3}{kg F_v}, \quad (6)$$

where ρ is density, θ_v is virtual potential temperature, $u_* = \sqrt{\tau/\rho}$ is friction velocity, k is the von Kármán constant, $F_v = S_0 + 0.61c_p T E_0$ is buoyancy flux, and τ is shear stress at the surface. Weckwerth et al. (1999) suggest that HCRs are favored when $-z_i/L < 25$ [i.e., when low-level wind shear is relatively strong (L relatively large)], while cells are favored for larger ratio values, such as for relatively large surface buoyancy flux or weak wind speeds. Calculating L from (6) using *Revelle* flux site measurements, and taking z_i as mixed-layer depth analyzed subjectively (Johnson et al. 2001) from

Revelle soundings, reveals mean ratio values of ~ 5 for the October suppressed period and ~ 130 for the November period. Therefore, conditions generally favor HCRs in the October period and open cells in the November period, owing to stronger low-level winds in SP–MJO1, both from the perspective of the *Revelle* (Fig. 8) and the greater sounding array (Johnson and Ciesielski 2013, their Fig. 12). While the role of evaporatively generated cold pools in the observed organization is yet unclear, it is likely that some of the cellular structures depicted in Figs. 12 and 13 owe to outward-spreading cold pools, particularly late in the suppressed phases as rainfall increases leading up to MJO onset (Figs. 2, 6, and 9–11) (Rowe and Houze 2014). Detailed observations of the boundary layer thermodynamics will be necessary to pin this down.

Weckwerth et al. (1996) show that the boundary layer circulation related to such mesoscale organization augments the convective instability in the boundary layer by creating localized areas of enhanced moisture, thereby promoting deeper convective clouds than would otherwise occur. Therefore, the cloud organization depicted in Figs. 12 and 13 reflects a process by which mesoscale circulation enhances the overall communication of

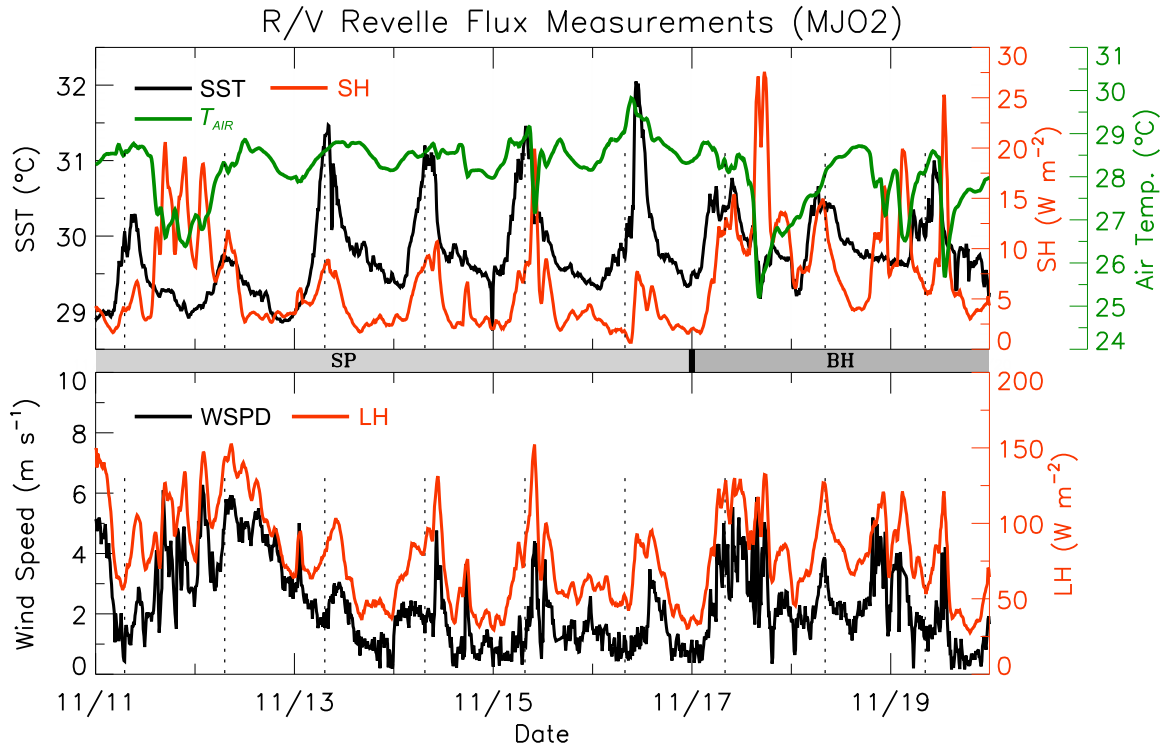


FIG. 10. As in Fig. 9, but for MJO2.

moisture between the boundary layer and overlying free troposphere.

Also apparent during both suppressed periods is a slight change in the cloud scenes within the 3 h between satellite overpasses each day. Specifically, an increase in the size and/or number of clouds by afternoon suggests that moist convection is intensifying. This change is particularly clear on 11, 12, and 14 October (Figs. 12c–h) and 11, 13, and 15 November (Figs. 13a,b,e–h) (note, however, that expanding cirrus cloud shields also influence the scenes in Figs. 12g,h and 13g,h). Diurnal composites of echo-top frequency and echo area coverage calculated from the S-PolKa RHI dataset (cf. section 2) are shown for segments of the suppressed phase in MJO1 (7–13 October) and MJO2 (13–16 November) in Fig. 14 (date ranges selected to avoid variability unrelated to the diurnal cycle; cf. Fig. 6). During both suppressed periods, echo-top frequency generally peaks in the lower troposphere, reflecting the dominance of shallow cumuli, with echo area coverage ranging approximately from 0% to 25%. An increase in low-level echo-top frequency occurs, however, as echo area coverage begins to increase around 1100 L during the October period (Fig. 14a) and ~0900 L in the November period (Fig. 14b), followed by a pronounced deepening of echo tops thereafter. Frequency > 0.5% reaches ~9–11 km as echo area peaks around 20% by

1500 L in both periods, indicating a midafternoon population of congestus clouds with larger cloud size and/or quantity than earlier in the day. This afternoon invigoration of clouds occurs on a large scale, as inferred from the morning to afternoon changes in the MODIS cloud scenes described above (Figs. 12 and 13). Bellenger et al. (2010) relate this afternoon convective invigoration to a reduction of convective inhibition, which is in turn driven by the boundary layer warming driven by increased SST. The deeper clouds persist through evening in the October period, dissipating around 0200 L. During the November period, however, deep overnight convective clouds appear more distinctly from afternoon convection, in both echo-top frequency and echo area coverage, around ~0000–0500 L.

Diurnal composites of TRMM rainfall averaged over the northern sounding array for periods in MJO1 (7–13 October) and MJO2 (11–16 November) are provided in Fig. 15. While the mean amounts are very small, both periods exhibit increasing rainfall in the afternoon in connection with building convection (Fig. 14). Afternoon rainfall peaks around 1700–2100 L, roughly around the time of greatest and deepest cloud echo-top frequency—a relationship that holds on the much longer time scale of the MJO (Xu and Rutledge 2014). While rainfall in the October period largely persists through night before tapering off in the morning (Fig. 15a), rainfall

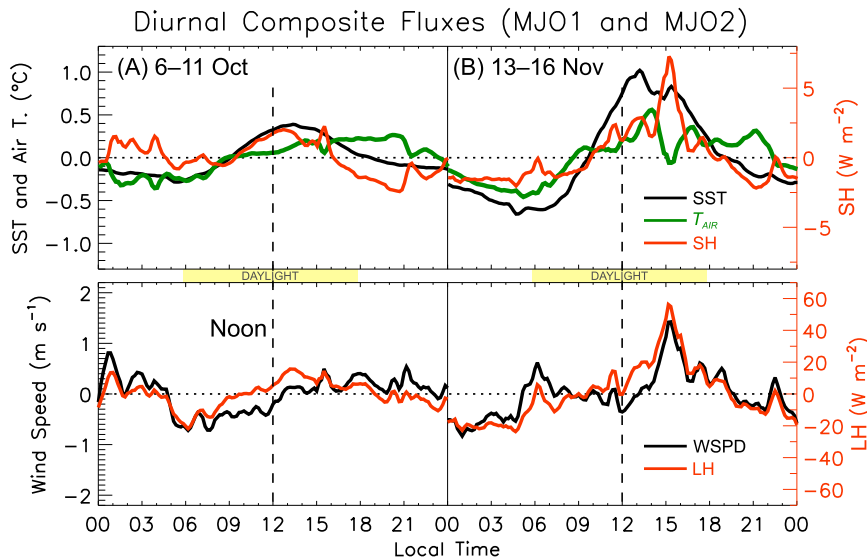


FIG. 11. (top) Diurnal composite SST (black; $^{\circ}\text{C}$; left axis), 10-m air temperature (green; $^{\circ}\text{C}$; left axis), and SH (red; W m^{-2} ; right axis) for the (a) October (MJO1) and (b) November (MJO2) suppressed phases. Composite means have been removed. (bottom) As in (top), but for wind speed (black; m s^{-1} ; left axis) and LH (red; W m^{-2} ; right axis). Composite date ranges are (a) 6–11 Oct and (b) 13–16 Nov (end dates are inclusive). Local time is indicated along the abscissa. Vertical dashed lines indicate local noon. All fields have been smoothed using a 30-min running mean. Yellow boxes indicate solar daylight hours, here and henceforth.

in the November period exhibits a more distinct early-morning maximum offset by ~ 12 h from the afternoon peak (Fig. 15b). This maximum in the November period is consistent with the distinct early-morning maximum in echo-top frequency and echo coverage (Fig. 14), though the timing is in slight disagreement. Differences in timing between Figs. 14 and 15 may relate to differences in spatial sampling between S-PolKa and the TRMM northern-array average (also recall the difference in sampling frequency). The existence of both afternoon and nocturnal rainfall peaks was also found in suppressed periods during COARE and MISMO (Sui et al. 1997; Johnson et al. 2001; Bellenger et al. 2010).

Figure 16 provides diurnal composite q , ω , Q_1 , and Q_2 derived from the DYNAMO gridded analysis for the suppressed phases in MJO1 (7–13 October) and MJO2 (11–16 November). Mixing ratio q is shown with the composite mean removed (q'), though the means are retained in all of the other fields. There is remarkable consistency in the diurnal cycle between the October and November suppressed phases, despite a relatively weaker diurnal cycle in fluxes during SP-MJO1, as measured at the *Revelle* (Figs. 9–11). Both periods exhibit a morning–evening q' swing of magnitude $\sim (0.4\text{--}0.6) \text{ g kg}^{-1}$ in the layer $\sim (900\text{--}550) \text{ hPa}$, with moister conditions in the evening. Since temperature varies negligibly (not shown), this diurnal variation in q'

directly correlates with relative humidity, which exhibits anomalies of $O(3\%)$. Most of the variation in q' occurs below the 0°C level, reflecting the dominance of warm-rain clouds (Figs. 6 and 14). Anomalies of q' do appear above the 0°C level overnight, however, which is indicative of deeper clouds (Fig. 14). The diurnal variation in ω indicates enhanced deep subsidence in the late evening–early morning, which may relate to the remote forcing of nocturnally invigorated deep convection in the ITCZ or elsewhere, though this issue remains unsolved. The weak rising motion (SP-MJO1; Fig. 16a) or relaxed subsidence (SP-MJO2; Fig. 16b) in the lower troposphere in the morning–afternoon likely owes to the local increase in convective activity. The evolution of Q_1 largely reflects the diurnal cycle of radiative heating, though enhanced warming near and within the boundary layer relates to the large convergence of eddy heat flux due to surface warming as the mixed layer deepens (Johnson et al. 2001).

The diurnal cycle in Q_2 indicates pronounced daytime apparent moistening, the majority of it taking place $\sim 0900\text{--}1800 \text{ L}$, which is in quadrature with q' , indicating the dominance of the local tendency term in (2) (this was verified by a check of the individual contributions to Q_2 ; not shown). Since $Q_2 < 0$ through most of the column, and precipitation is negligible (Fig. 2), this signal can be related back to the vertical convergence of vertical eddy

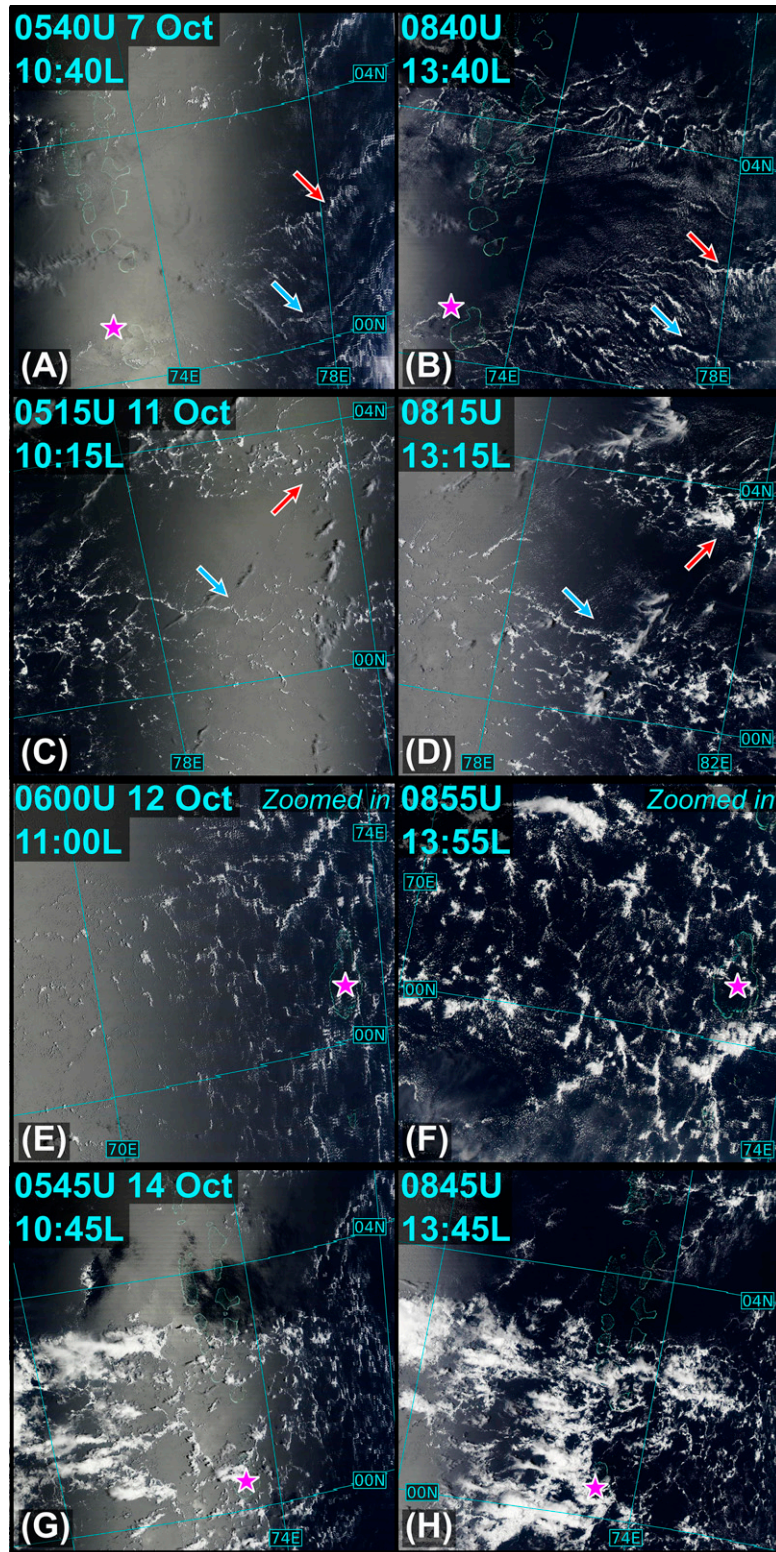


FIG. 12. Cropped true-color images from the (a),(c),(e),(g) *Terra* and (b),(d),(f),(h) *Aqua* MODIS satellites for selected dates of the October suppressed phase (MJO1). Date is indicated in the left column, and UTC and local time are indicated in each panel. The magenta star marks Huvadhu Atoll, located ~ 100 km north of Addu Atoll (i.e., Gan Island). Red and blue arrows indicate subjectively identified corresponding cloud features between same-day images.

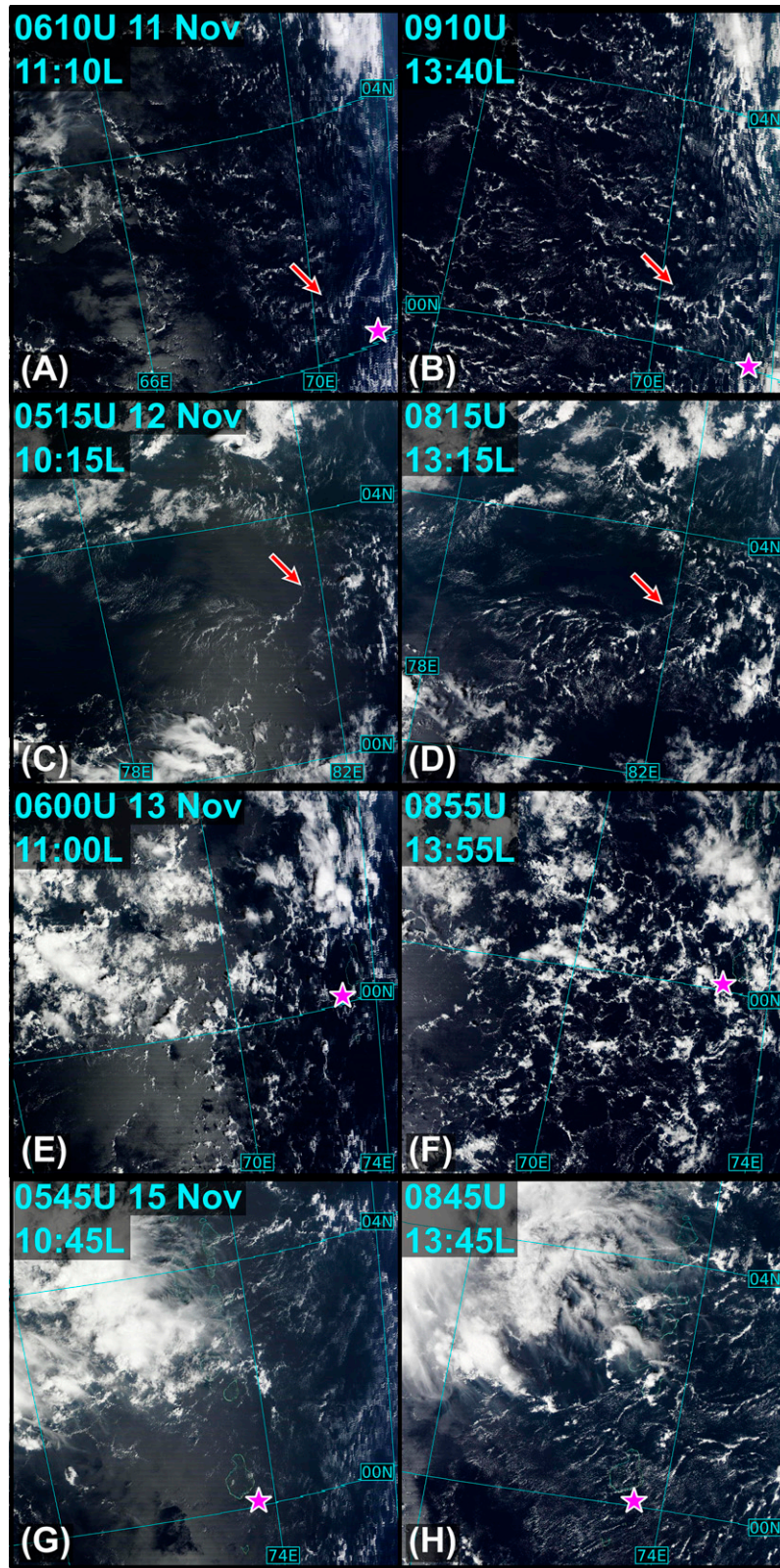


FIG. 13. As in Fig. 12, but for the November suppressed phase (MJO2).

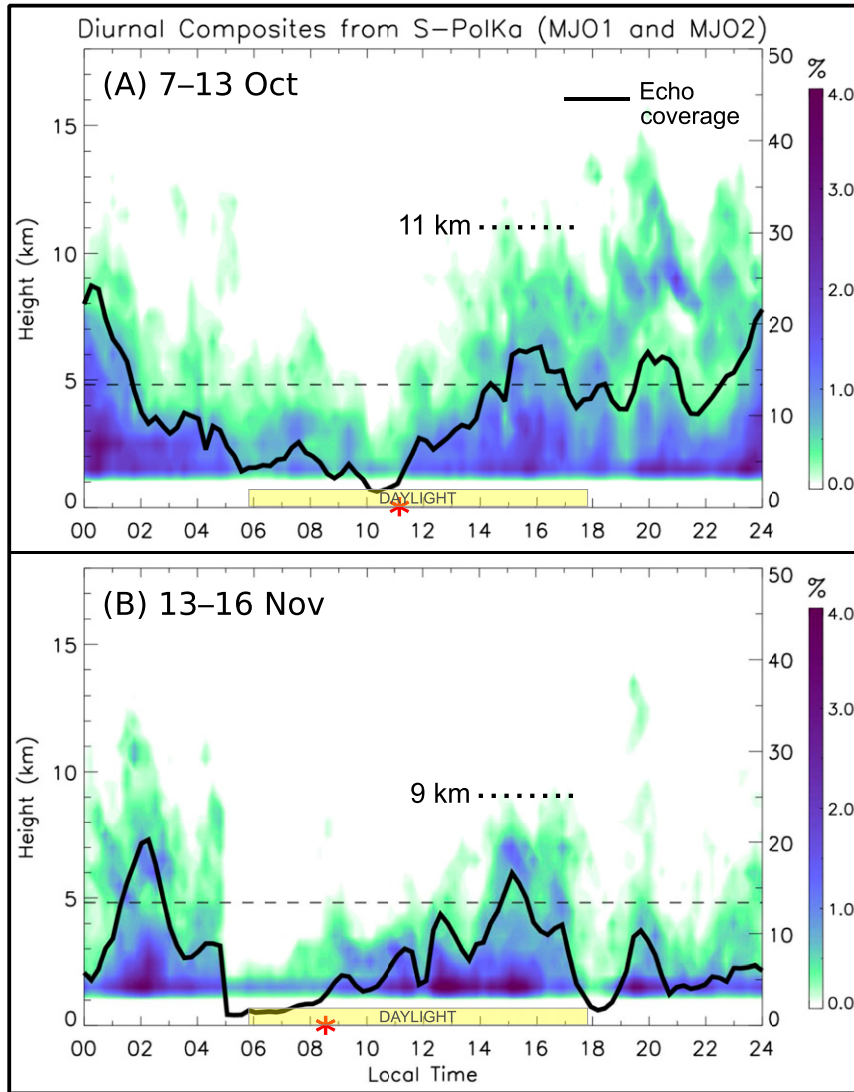


FIG. 14. Diurnal time–height composites of convective echo-top frequency (shading; %) and echo area coverage (solid black line; %; right axis) for the (a) October and (b) November suppressed phases, calculated from 15-min S-PolKa RHI data (see section 2 for methodology). Composite date ranges are (a) 7–13 Oct and (b) 13–16 Nov (end dates are inclusive). Local time is indicated along the abscissa. Red asterisks mark the time of increasing echo-top frequency and echo area coverage. The 11- and 9-km levels are indicated by dotted lines in (a) and (b), respectively. Horizontal dashed lines indicate the 0°C level.

moisture flux, which ties to surface evaporation [Eqs. (2) and (4)]. This conclusion also follows by noting the magnitude difference between Q_1 and Q_2 : if water phase changes dominated the moisture source, Q_1 and Q_2 would exhibit similar magnitude (such as when stratiform rainfall abounds, as in the active phase; Fig. 3). Therefore, while latent heat release in the cloud layer is critical for driving convective eddies upward into the free troposphere, it is the large vertical eddy moisture flux by clouds that is driving this moistening. Moistening in Q_2 reaches a peak of $\sim 10 \text{ K day}^{-1}$ ($\sim 4 \text{ g kg}^{-1} \text{ day}^{-1}$)

at 1400 L around 800 hPa in the October period, which closely coincides with the time of peak $L_v E_0$ as measured at the *Revelle* (Fig. 11; recall the difference in temporal resolution between these two datasets). While Q_2 moistening persists within a shallow layer through much of the evening in SP/MJO1, Q_2 switches to drying overnight–early morning during SP–MJO2. A cycle in q' and Q_2 also appears in the boundary layer (i.e., below $\sim 900 \text{ hPa}$), which is shifted slightly later than the cycle in the free troposphere. While this boundary layer moistening is not yet understood, it has been observed in

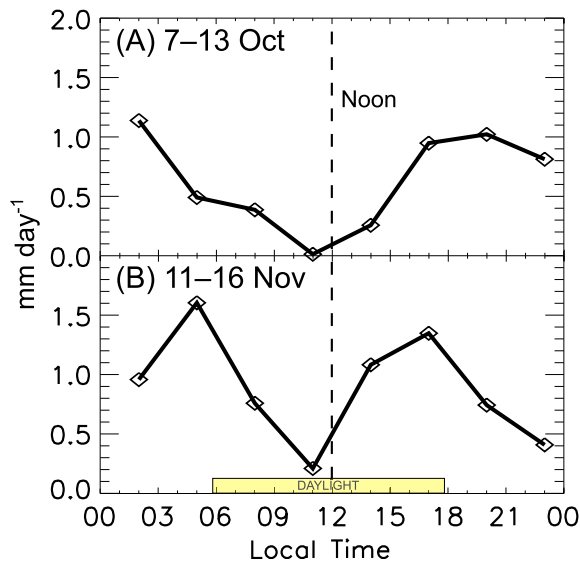


FIG. 15. Diurnal composites of TRMM 3B42 rainfall (mm day^{-1}) averaged over the northern sounding quadrilateral for the (a) October and (b) November suppressed phases. Composite date ranges are (a) 7–13 Oct and (b) 11–16 Nov (end dates are inclusive). Local time is indicated along the abscissa.

previous field campaigns (Sui et al. 1997; Yasunaga et al. 2008).

An issue that remains unresolved is the role of water vapor storage in clouds: since the volume of clouds exhibits substantial diurnal fluctuation (Fig. 14), the amount of water contained in suspended hydrometeors likely also fluctuates (McNab and Betts 1978). This issue will be the subject of a future study. Another present hurdle to closing the moisture budget on the diurnal time scale is that accurate diurnal surface flux information is limited to a single location (e.g., Fig. 11), while information over the northern sounding array is necessary to complement the sounding-derived information (Fig. 16).

The findings described in this section demonstrate that the locally driven diurnal cycle explains much of the temporal variation in column humidity over the DYNAMO northern sounding array, as demonstrated during the period of low–midlevel moistening in the suppressed phase or preonset stage of the MJO (Fig. 7). This diurnal cycle is characterized by a daytime deepening of clouds from shallow cumulus to congestus, an increase in their areal coverage, and a corresponding peak in cumulus moistening (Figs. 7 and 12–16). The afternoon invigoration of convection is driven by the afternoon peak in SST and air–sea fluxes, which owes to the influence of oceanic diurnal warm layers (Figs. 8–11) (Bellenger et al. 2010; Matthews et al. 2014). The correspondence in the diurnal cycle between the key

observational platforms described in this study is demonstrated in a supplemental figure (file JAS-D-14-0218s1 in the supplementary material).

A noteworthy finding described in this section is the prominence of mesoscale cloud organization during the suppressed phase (also observed in COARE; Fig. 8 of Johnson et al. 2001), which is manifest in HCRs and/or open cells, depending primarily on the strength of the low-level wind (Figs. 12 and 13). This cloud organization is indicative of buoyancy-driven boundary layer overturning circulation, which is likely important for augmenting the overall communication of moisture between the boundary layer and the overlying free troposphere (Weckwerth et al. 1996).

5. Summary and conclusions

Two MJO events were comprehensively sampled in the tropical Indian Ocean during DYNAMO, providing an unprecedented opportunity to diagnose the key processes in the transition from shallow to deep moist convection during MJO convective onset from in situ measurements. Atmospheric soundings, radar, and air–sea flux measurements collected during DYNAMO have been employed to carry out this diagnosis.

The findings of section 3—a large-scale overview of two DYNAMO MJO events—demonstrate that humidification of the low–midtroposphere during the late-suppressed phase or preonset stage of the MJO owed to simultaneous changes in the convective cloud population and large-scale circulation, as schematically depicted in Fig. 17a [note: the clouds depicted in Fig. 17 represent the predominant character of the convective cloud population; all convective cloud modes, however, can occur within a given MJO phase (Mapes et al. 2006; Barnes and Houze 2013)]. While there were differences between the preonset stage of MJO1 and that of MJO2 (i.e., the character and duration of moistening and depth of the moist layer; Fig. 2), the role of large-scale circulation is similar in both. Namely, the drying by large-scale circulation wanes as the low–midtroposphere humidifies and the convective cloud population is invigorated (Fig. 17a). Rainfall begins and increases as the column is moistened and convective clouds deepen. Following MJO onset (i.e., the onset of large-scale diabatic heating; Fig. 3), humidity is increased over the full depth of the column in connection with relatively bottom-heavy convection, which is indicative of predominant congestus and cumulonimbus clouds and minimal stratiform rainfall. The heating profile becomes progressively more top heavy as peak ascending motion shifts upward later in the active phase, indicating

Diurnal Composites from Budgets (MJO1 and MJO2)

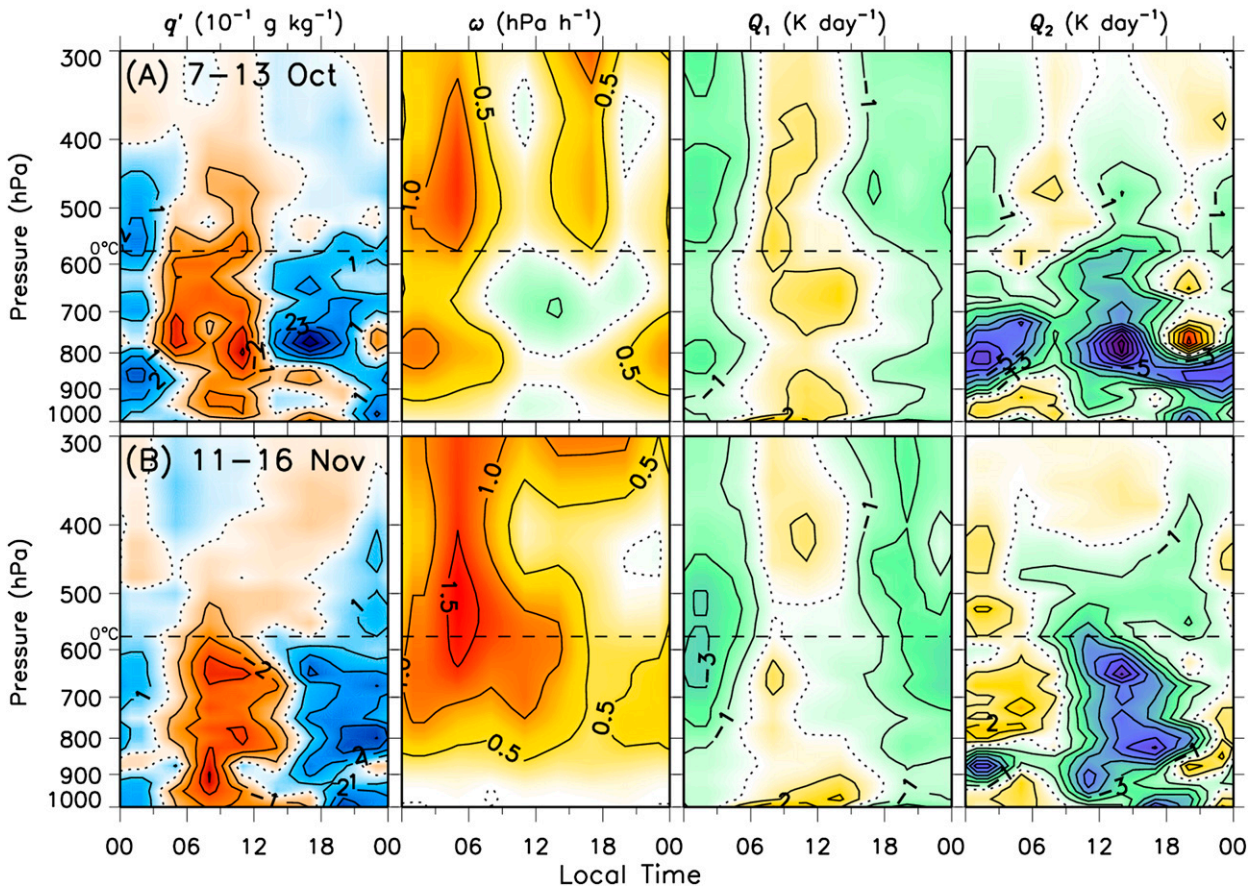


FIG. 16. Diurnal composite variables from the northern-array gridded analysis for the suppressed phases of (a) MJO1 and (b) MJO2, showing (left to right) water vapor mixing ratio with composite mean removed q' (contoured every $10^{-1} \text{ g kg}^{-1}$), ω (every 0.5 hPa h^{-1}), Q_1 , and Q_2 (every K day^{-1}). Positive values are shaded in red, except for q' , where red is negative. Composite date ranges are (a) 7–13 Oct and (b) 11–16 Nov (end dates are inclusive). Horizontal dashed lines indicate the 0°C level. Vertical smoothing has been applied to all fields using a three-point running mean.

increasing stratiform rainfall. This evolution is generally consistent with the findings of previous studies (Maloney and Hartmann 1998; Johnson et al. 1999; Benedict and Randall 2007; Riley et al. 2011; Del Genio et al. 2012; Barnes and Houze 2013; Powell and Houze 2013; Zuluaga and Houze 2013; Kerns and Chen 2014; Rowe and Houze 2014; Xu and Rutledge 2014).

The moisture budget indicates the importance of both vertical and horizontal advection in the moistening of the low–midtroposphere prior to and during MJO convective onset—namely, via relaxation of the drying due to subsidence and horizontal advection. The role of horizontal advection in DYNAMO is largely manifest in a waxing and waning of horizontal-advective drying, which relates to the enhancement (abatement) of low-level westerly flow (Fig. 17a) and equatorial Rossby

gyres during the active phase (preonset stage) (Gottschalck et al. 2013; Kerns and Chen 2014). The abatement of subsidence drying during the preonset stage is partly linked to the approach of the global-circumnavigating (gravity or Kelvin wave) MJO signal, which drives a relaxation of upper-level convergence (Kiladis et al. 2001; Gottschalck et al. 2013; Johnson and Ciesielski 2013). The appearance of high cirrus clouds prior to MJO onset is also linked to the near-tropopause adiabatic cooling and moistening driven by this circumnavigating signal (Fig. 17a) (Virts and Wallace 2010; Virts et al. 2010; Riley et al. 2011; Del Genio et al. 2012).

Local factors may also be important for the observed waning of subsidence. In particular, column radiative cooling is observed to decrease during the preonset stage (Johnson et al. 2015; Sobel et al. 2014), which coincides with the invigoration of convective clouds and

MJO Convective Onset in the Indian Ocean

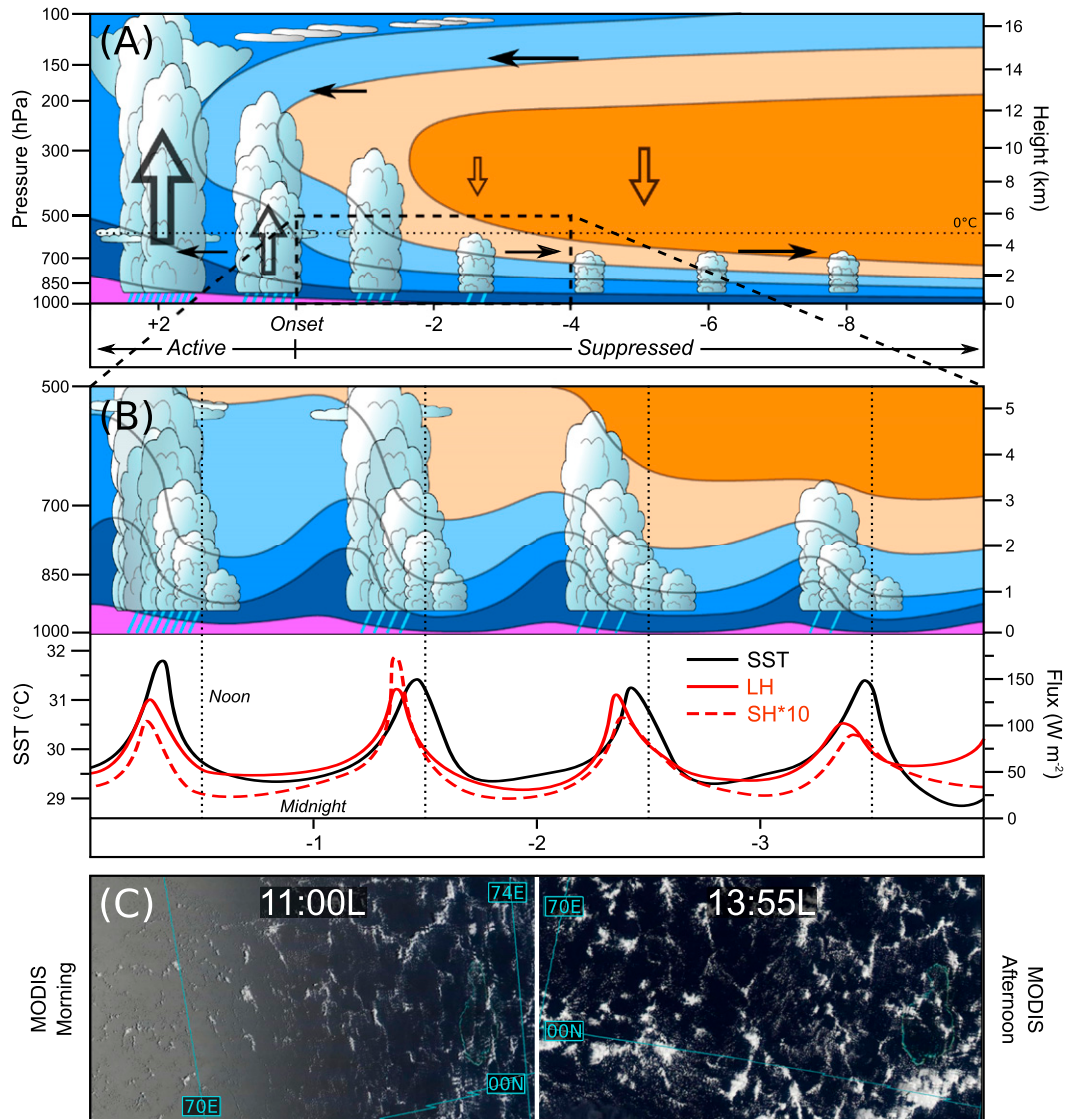


FIG. 17. A schematic model of MJO convective onset in the tropical Indian Ocean, depicted in an Eulerian framework with time (days leading up to MJO onset) from right to left. (a) Time–pressure pictorial of convective clouds (i.e., their predominant character), relative humidity (RH; shading; range is ~40%–80%; brown is drier), and rainfall (blue lines) from the suppressed phase through onset to the early-active phase. Depicted is a transition from shallow cumulus to congestus to deep cumulonimbus and stratiform clouds, with high cirrus clouds appearing prior to onset, as the troposphere moistens and rainfall intensifies. Open (solid) arrows depict vertical (horizontal) motion, with size proportional to magnitude. (b) (top) Time–pressure series emphasizing diurnal variability during the late-suppressed phase or preonset stage [time–pressure space denoted by the dashed box in (a)], with RH, convective clouds, and rainfall; and (bottom) the corresponding time series of SST (black), latent heat flux (LH; red, solid), and sensible heat flux (SH) multiplied by 10 (red, dashed). Abscissa ticks are local midnight, and vertical dotted lines are local noon. (c) Characteristic cloud field during the suppressed phase as depicted by MODIS true-color imagery in the (left) morning (0600 UTC, 1100 L) and (right) afternoon (0855 UTC, 1355 L) (from 12 Oct 2011; Figs. 12e,f), revealing the prominence of mesoscale cloud organization (i.e., open cells and horizontal convective rolls).

development of high cirrus clouds. Reduced column radiative cooling must in turn cause relaxation of the large-scale subsidence when assuming negligible temperature variations (Mapes 2001). While such

a feedback between moist-convective clouds, column radiative heating, and large-scale subsidence is cited as a maintenance mechanism for the MJO active phase in the context of moisture-mode theory (Chikira 2014), it is

possible that this feedback also plays a role in the transition from shallow to deep convection during MJO onset/initiation.

DYNAMO observations have also been exploited to describe the diurnal cycle of moist convection during the suppressed phase or preonset stage of the two MJO events (section 4), with the aim of improving our understanding of the physical processes involved in convective invigoration and, ultimately, shedding light on convective invigoration in relation to MJO onset. A new finding of this study is the importance of the locally driven diurnal cycle during the preonset stage of the MJO. Namely, the diurnal cycle of convective clouds dominates temporal variations of column humidity during the preonset stage (Fig. 7). This diurnal cycle is characterized by a daytime deepening of shallow cumuli (and an increase in their areal coverage; Fig. 14), which develop into congestus clouds by afternoon. This diurnal cycle is schematically depicted in Fig. 17b (top panel), which occurs within the slower (i.e., daily mean) evolution associated with the transition into the MJO active phase (Fig. 17a). This daily convective invigoration drives a prominent daytime maximum in cumulus moistening (Fig. 16), which roughly coincides with a peak in SST and air–sea fluxes—the fluxes lagging the SST maxima by approximately 2 h (Fig. 17b, bottom panel). The diurnal cycle in SST relates to oceanic diurnal warm layers that form under light-wind, clear-sky conditions (Halpern and Reed 1976; Matthews et al. 2014). This daytime surface warming drives an increase in surface fluxes, which invigorates moist convection by reducing convective inhibition (Fig. 11; Bellenger et al. 2010). Figure 17b schematically depicts this ocean-driven diurnal moistening and diurnal cloud response within an environment that is transitioning from suppressed to active conditions in connection with MJO onset—that is, as the drying by large-scale subsidence and horizontal advection wanes and convective clouds deepen in the daily-mean sense (Fig. 17a). The correspondence of various fields over the course of the diurnal cycle is also demonstrated in a supplemental figure, which recombines information from several datasets described in section 4.

A further finding of this study is the prominence of mesoscale cloud organization during the suppressed phase, which is manifest in open cells and horizontal convective rolls (Fig. 17c). The character of this organization relates to the relative magnitudes of shear-driven and buoyancy-driven turbulence, though it fundamentally owes to heating from below by the warm ocean surface. This mesoscale organization may play a role in the moistening process by driving convective elements to greater heights than would otherwise occur through

the local enhancement of convergence and deepening of boundary layer moisture along cell boundaries (Weckwerth et al. 1996). More work is needed to investigate this process and ascertain the relative role of cold pools in the organization.

The primary findings of this study lead to two new testable hypotheses pertaining to the transition from the suppressed to the active phase of the MJO:

- 1) The diurnal cycle of sea surface temperature and air–sea fluxes drive a net boost to convective activity and cumulus moistening in the low–midtroposphere, which would not exist without such a diurnal cycle. That is to say, the daytime invigoration of moist convection related to the diurnal cycle of SST yields more vigorous cumulus convection in a daily-mean sense than if this diurnal cycle did not exist. If this hypothesis were true, then the diurnal cycle of SST, as described herein, may be regarded as a forcing mechanism for convective invigoration and column moistening.
- 2) The mesoscale organization of clouds and the associated mesoscale circulation lead to localized areas of enhanced boundary layer moisture and deeper mixed layers (Weckwerth et al. 1996; Johnson et al. 2001), leading to deeper clouds than would otherwise occur. This hypothesis is analogous to the former in that it brings to light the possible role of local processes (i.e., mesoscale cloud organization) in augmenting cumulus moistening of the low–midtroposphere and, hence, assisting the transition from shallow to deeper convective clouds during MJO convective onset.

Proper testing of these hypotheses using models will require, at a minimum, simultaneous resolution of both the cumulus scale, $O(\leq 500\text{ m})$, and the mesoscale cloud organization, $O(>10\text{ km})$ (Figs. 12 and 13).

Recent studies demonstrate that the diurnal cycle of SST in the tropics, wherein the heat received during the day in the shallow warm layer is convectively mixed downward overnight, is critical to rectifying the slower (i.e., daily mean) SST increase during the suppressed phase of the MJO (Fig. 8; Webster et al. 1996; Duvel et al. 2004; Bernie et al. 2005, 2008; Vialard et al. 2009; Matthews et al. 2014). While it is yet undetermined whether this intraseasonal SST increase is important to the MJO, it is plausible that this diurnal cycle in SST, and the diurnal cycle in clouds that it drives, is key to rectifying the moistening of the low–midtroposphere during the preonset stage of the MJO. This possible link, which underpins hypothesis 1 above, could have major implications for both modeling and basic understanding of the MJO. The diurnal cycle in the

tropical atmosphere is clearly an open subject in need of greater investigation.

Acknowledgments. We greatly acknowledge Paul Ciesielski [Colorado State University (CSU)] for the processing of the DYNAMO sounding dataset; the Robert Houze research group (University of Washington), Zhe Feng (ARM–Pacific Northwest National Laboratory), and the NCAR Earth Observing Laboratory for their efforts with the S-PolKa dataset; and Jim Edson (University of Connecticut), Chris Fairall (Earth System Research Laboratory Physical Sciences Division), and Simon De Szoeke (Oregon State University) for their efforts with the air–sea flux dataset. We acknowledge many colleagues for insightful discussions of this work, especially Paul Ciesielski, Charlotte DeMott, Alex Gonzalez, Walter Hannah, Elizabeth Thompson, and Brandon Wolding from CSU. The comments of three anonymous reviewers substantially improved the clarity of this study. Chidong Zhang (University of Miami) and all other participants in DYNAMO/CINDY/AMIE/LASP are greatly acknowledged. This research has been supported by the National Science Foundation under Grants AGS-1059899, AGS-1138353, and AGS-1360237, the National Aeronautics and Space Administration under Grant NNX13AF74G, and the Department of Energy Grant DE-SC0008582.

REFERENCES

- Arakawa, A., and W. H. Schubert, 1974: Interaction of a cumulus cloud ensemble with the large-scale environment, Part I. *J. Atmos. Sci.*, **31**, 674–701, doi:10.1175/1520-0469(1974)031<0674:IOACCE>2.0.CO;2.
- Austin, J. M., 1948: A note on cumulus growth in a non-saturated environment. *J. Meteor.*, **5**, 103–107, doi:10.1175/1520-0469(1948)005<0103:ANOCGI>2.0.CO;2.
- Barnes, H. C., and R. A. Houze Jr., 2013: The precipitating cloud population of the Madden-Julian Oscillation over the Indian and west Pacific Oceans. *J. Geophys. Res. Atmos.*, **118**, 6996–7023, doi:10.1002/jgrd.50375.
- Bellenger, H., Y. N. Takayabu, T. Ushiyama, and K. Yoneyama, 2010: Role of diurnal warm layers in the diurnal cycle of convection over the tropical Indian Ocean during MISO. *Mon. Wea. Rev.*, **138**, 2426–2433, doi:10.1175/2010MWR3249.1.
- Benedict, J. J., and D. A. Randall, 2007: Observed characteristics of the MJO relative to maximum rainfall. *J. Atmos. Sci.*, **64**, 2332–2354, doi:10.1175/JAS3968.1.
- Bernie, D. J., S. J. Woolnough, J. M. Slingo, and E. Guilyardi, 2005: Modeling diurnal and intraseasonal variability of the ocean mixed layer. *J. Climate*, **18**, 1190–1202, doi:10.1175/JCLI3319.1.
- , E. Guilyardi, G. Madec, J. M. Slingo, S. J. Woolnough, and J. Cole, 2008: Impact of resolving the diurnal cycle in an ocean–atmosphere GCM. Part 2: A diurnally coupled CGCM. *Climate Dyn.*, **31**, 909–925, doi:10.1007/s00382-008-0429-z.
- Bladé, I., and D. L. Hartmann, 1993: Tropical intraseasonal oscillations in a simple nonlinear model. *J. Atmos. Sci.*, **50**, 2922–2939, doi:10.1175/1520-0469(1993)050<2922:TIOIAS>2.0.CO;2.
- Charney, J. G., 1963: A note on large-scale motions in the tropics. *J. Atmos. Sci.*, **20**, 607–609, doi:10.1175/1520-0469(1963)020<0607:ANOLSM>2.0.CO;2.
- Chen, S. S., and R. A. Houze Jr., 1997: Diurnal variation and life-cycle of deep convective systems over the tropical Pacific warm pool. *Quart. J. Roy. Meteor. Soc.*, **123**, 357–388, doi:10.1002/qj.49712353806.
- , —, and B. E. Mapes, 1996: Multiscale variability of deep convection in relation to large-scale circulation in TOGA COARE. *J. Atmos. Sci.*, **53**, 1380–1409, doi:10.1175/1520-0469(1996)053<1380:MVODCI>2.0.CO;2.
- Chikira, M., 2014: Eastward-propagating intraseasonal oscillation represented by Chikira–Sugiyama cumulus parameterization. Part II: Understanding moisture variation under weak temperature gradient balance. *J. Atmos. Sci.*, **71**, 615–639, doi:10.1175/JAS-D-13-038.1.
- Ciesielski, P. E., R. H. Johnson, P. T. Haertel, and J. Wang, 2003: Corrected TOGA COARE sounding humidity data: Impact on diagnosed properties of convection and climate over the warm pool. *J. Climate*, **16**, 2370–2384, doi:10.1175/2790.1.
- , —, K. Yoneyama, and R. K. Taft, 2014a: Mitigation of Sri Lanka island effects in Colombo sounding data and its impact on DYNAMO analyses. *J. Meteor. Soc. Japan*, **92**, 385–405, doi:10.2151/jmsj.2014-407.
- , and Coauthors, 2014b: Quality-controlled upper-air sounding dataset for DYNAMO/CINDY/AMIE: Development and corrections. *J. Atmos. Oceanic Technol.*, **31**, 741–764, doi:10.1175/JTECH-D-13-00165.1.
- Dai, A., 2001: Global precipitation and thunderstorm frequencies. Part II: Diurnal variations. *J. Climate*, **14**, 1112–1128, doi:10.1175/1520-0442(2001)014<1112:GPATFP>2.0.CO;2.
- Davison, J. L., R. M. Rauber, and L. Di Girolamo, 2013: A revised conceptual model of the tropical marine boundary layer. Part II: Detecting relative humidity layers using Bragg scattering from S-Band radar. *J. Atmos. Sci.*, **70**, 3025–3046, doi:10.1175/JAS-D-12-0322.1.
- Del Genio, A. D., Y. Chen, D. Kim, and M.-S. Yao, 2012: The MJO transition from shallow to deep convection in *CloudSat*/CALIPSO data and GISS GCM simulations. *J. Climate*, **25**, 3755–3770, doi:10.1175/JCLI-D-11-00384.1.
- DeMott, C. A., and S. A. Rutledge, 1998: The vertical structure of TOGA COARE convection. Part II: Modulating influences and implications for diabatic heating. *J. Atmos. Sci.*, **55**, 2748–2762, doi:10.1175/1520-0469(1998)055<2748:TVSOTC>2.0.CO;2.
- Derbyshire, S. H., I. Beau, P. Bechtold, J.-Y. Grandpeix, J.-M. Piriou, J.-L. Redelsperger, and P. M. M. Soares, 2004: Sensitivity of moist convection to environmental humidity. *Quart. J. Roy. Meteor. Soc.*, **130**, 3055–3079, doi:10.1256/qj.03.130.
- Duvel, J. P., R. Roca, and J. Vialard, 2004: Ocean mixed layer temperature variations induced by intraseasonal convective perturbations over the Indian Ocean. *J. Atmos. Sci.*, **61**, 1004–1023, doi:10.1175/1520-0469(2004)061<1004:OMLTVI>2.0.CO;2.
- Feng, Z., S. A. McFarlane, C. Schumacher, S. Ellis, J. Comstock, and N. Bharadwaj, 2014: Constructing a merged cloud–precipitation radar dataset for tropical convective clouds during the DYNAMO/AMIE experiment at Addu Atoll. *J. Atmos. Oceanic Technol.*, **31**, 1021–1042, doi:10.1175/JTECH-D-13-00132.1.

- Flament, P., J. Firing, M. Sawyer, and C. Trefois, 1994: Amplitude and horizontal structure of a large diurnal sea surface warming event during the Coastal Ocean Dynamics Experiment. *J. Phys. Oceanogr.*, **24**, 124–139, doi:10.1175/1520-0485(1994)024<0124:AAHSOA>2.0.CO;2.
- Gill, A. E., 1980: Some simple solutions for heat-induced tropical circulation. *Quart. J. Roy. Meteor. Soc.*, **106**, 447–462, doi:10.1002/qj.49710644905.
- Gottschalck, J., P. E. Roundy, C. J. Schreck III, A. Vintzileos, and C. Zhang, 2013: Large-scale atmospheric and oceanic conditions during the 2011–12 DYNAMO field campaign. *Mon. Wea. Rev.*, **141**, 4173–4196, doi:10.1175/MWR-D-13-00022.1.
- Gray, W. M., and R. W. Jacobson, 1977: Diurnal variation of deep cumulus convection. *Mon. Wea. Rev.*, **105**, 1171–1188, doi:10.1175/1520-0493(1977)105<1171:DVODCC>2.0.CO;2.
- Haertel, P. T., G. N. Kiladis, A. Denno, and T. M. Rickenbach, 2008: Vertical-mode decompositions of 2-day waves and the Madden-Julian oscillation. *J. Atmos. Sci.*, **65**, 813–833, doi:10.1175/2007JAS2314.1.
- Halpern, D., and R. K. Reed, 1976: Heat budget of the upper ocean under light winds. *J. Phys. Oceanogr.*, **6**, 972–975, doi:10.1175/1520-0485(1976)006<0972:HBOTUO>2.0.CO;2.
- Hendon, H. H., and B. Liebmann, 1990: The intraseasonal (30–50 day) oscillation of the Australian summer monsoon. *J. Atmos. Sci.*, **47**, 2909–2924, doi:10.1175/1520-0469(1990)047<2909:TIDOOT>2.0.CO;2.
- , and M. L. Salby, 1994: The life cycle of the Madden-Julian oscillation. *J. Atmos. Sci.*, **51**, 2225–2237, doi:10.1175/1520-0469(1994)051<2225:TLCOTM>2.0.CO;2.
- , B. Liebmann, M. Newman, J. D. Glick, and J. E. Schemm, 2000: Medium-range forecast errors associated with active episodes of the Madden-Julian oscillation. *Mon. Wea. Rev.*, **128**, 69–86, doi:10.1175/1520-0493(2000)128<0069:MRFEAW>2.0.CO;2.
- Hohenegger, C., and B. Stevens, 2013: Preconditioning deep convection with cumulus congestus. *J. Atmos. Sci.*, **70**, 448–464, doi:10.1175/JAS-D-12-089.1.
- Huffman, G. J., R. F. Adler, D. T. Bolvin, G. Gu, E. J. Nelkin, K. P. Bowman, E. F. Stocker, and D. B. Wolff, 2007: The TRMM Multisatellite Precipitation Analysis (TMPA): Quasi-global, multiyear, combined-sensor precipitation estimates at fine scales. *J. Hydrometeorol.*, **8**, 38–55, doi:10.1175/JHM560.1.
- Jiang, X., and Coauthors, 2011: Vertical diabatic heating structure of the MJO: Intercomparison between recent reanalyses and TRMM estimates. *Mon. Wea. Rev.*, **139**, 3208–3223, doi:10.1175/2011MWR3636.1.
- Johnson, R. H., 2011: Diurnal cycle of monsoon convection. *The Global Monsoon System: Research and Forecasts*, 2nd ed. C.-P. Chang et al., Eds., World Scientific, 257–276.
- , and X. Lin, 1997: Episodic trade wind regimes over the western Pacific warm pool. *J. Atmos. Sci.*, **54**, 2020–2034, doi:10.1175/1520-0469(1997)054<2020:ETWROT>2.0.CO;2.
- , and P. E. Ciesielski, 2002: Characteristics of the 1998 summer monsoon onset over the northern South China Sea. *J. Meteor. Soc. Japan*, **80**, 561–578, doi:10.2151/jmsj.80.561.
- , and —, 2013: Structure and properties of Madden-Julian oscillations deduced from DYNAMO sounding arrays. *J. Atmos. Sci.*, **70**, 3157–3179, doi:10.1175/JAS-D-13-065.1.
- , T. M. Rickenbach, S. A. Rutledge, P. E. Ciesielski, and W. H. Schubert, 1999: Trimodal characteristics of tropical convection. *J. Climate*, **12**, 2397–2418, doi:10.1175/1520-0442(1999)012<2397:TCOTC>2.0.CO;2.
- , P. E. Ciesielski, and J. A. Cotturone, 2001: Multiscale variability of the atmospheric mixed layer over the western Pacific warm pool. *J. Atmos. Sci.*, **58**, 2729–2750, doi:10.1175/1520-0469(2001)058<2729:MVOTAM>2.0.CO;2.
- , —, T. S. L'Ecuyer, and A. J. Newman, 2010: Diurnal cycle of convection during the 2004 North American Monsoon Experiment. *J. Climate*, **23**, 1060–1078, doi:10.1175/2009JCLI3275.1.
- , —, J. H. Ruppert Jr., and M. Katsumata, 2015: Sounding-based thermodynamic budgets for DYNAMO. *J. Atmos. Sci.*, **72**, 598–622, doi:10.1175/JAS-D-14-0202.1.
- Katsumata, M., P. E. Ciesielski, and R. H. Johnson, 2011: Evaluation of budget analyses during MISMO. *J. Appl. Meteor. Climatol.*, **50**, 241–254, doi:10.1175/2010JAMC2515.1.
- Kawai, Y., and A. Wada, 2007: Diurnal sea surface temperature variation and its impact on the atmosphere and ocean: A review. *J. Oceanogr.*, **63**, 721–744, doi:10.1007/s10872-007-0063-0.
- Keeler, R. J., J. Lutz, and J. Vivekanandan, 2000: S-Pol: NCAR's polarimetric Doppler research radar. *Proc. IGARS 2000: IEEE 2000 Int. Geoscience and Remote Sensing Symp.*, Honolulu, HI, Vol. 4, IEEE, 1570–1573, doi:10.1109/IGARSS.2000.857275.
- Kemball-Cook, S. R., and B. C. Weare, 2001: The onset of convection in the Madden-Julian oscillation. *J. Climate*, **14**, 780–793, doi:10.1175/1520-0442(2001)014<0780:TOOCIT>2.0.CO;2.
- Kerns, B. W., and S. S. Chen, 2014: Equatorial dry air intrusion and related synoptic variability in MJO initiation during DYNAMO. *Mon. Wea. Rev.*, **142**, 1326–1343, doi:10.1175/MWR-D-13-00159.1.
- Kikuchi, K., and Y. N. Takayabu, 2004: The development of organized convection associated with the MJO during TOGA COARE IOP: Trimodal characteristics. *Geophys. Res. Lett.*, **31**, L10101, doi:10.1029/2004GL019601.
- Kiladis, G. N., K. H. Straub, G. C. Reid, and K. S. Gage, 2001: Aspects of interannual and intraseasonal variability of the tropopause and lower stratosphere. *Quart. J. Roy. Meteor. Soc.*, **127**, 1961–1983, doi:10.1002/qj.49712757606.
- , —, and P. T. Haertel, 2005: Zonal and vertical structure of the Madden-Julian oscillation. *J. Atmos. Sci.*, **62**, 2790–2809, doi:10.1175/JAS3520.1.
- Kummerow, C., and Coauthors, 2000: The status of the Tropical Rainfall Measuring Mission (TRMM) after two years in orbit. *J. Appl. Meteor.*, **39**, 1965–1982, doi:10.1175/1520-0450(2001)040<1965:TSOTTR>2.0.CO;2.
- Lin, J. L., and Coauthors, 2006: Tropical intraseasonal variability in 14 IPCC AR4 climate models. Part I: Convective signals. *J. Climate*, **19**, 2665–2690, doi:10.1175/JCLI3735.1.
- Lin, X., and R. H. Johnson, 1996a: Kinematic and thermodynamic characteristics of the flow over the western Pacific warm pool during TOGA COARE. *J. Atmos. Sci.*, **53**, 695–715, doi:10.1175/1520-0469(1996)053<0695:KATCOT>2.0.CO;2.
- , and —, 1996b: Heating, moistening, and rainfall over the western Pacific warm pool during TOGA COARE. *J. Atmos. Sci.*, **53**, 3367–3383, doi:10.1175/1520-0469(1996)053<3367:HMAROT>2.0.CO;2.
- Liu, C., E. J. Zipser, and S. W. Nesbitt, 2007: Global distribution of tropical deep convection: Different perspectives from TRMM infrared and radar data. *J. Climate*, **20**, 489–503, doi:10.1175/JCLI4023.1.
- Madden, R. A., and P. R. Julian, 1971: Detection of a 40–50 day oscillation in the zonal wind in the tropical Pacific. *J. Atmos. Sci.*, **28**, 702–708, doi:10.1175/1520-0469(1971)028<0702:DOADOI>2.0.CO;2.

- , and —, 1972: Description of global-scale circulation cells in the tropics with a 40–50 day period. *J. Atmos. Sci.*, **29**, 1109–1123, doi:10.1175/1520-0469(1972)029<1109:DOGSCC>2.0.CO;2.
- Majda, A. J., and S. N. Stechmann, 2009: The skeleton of tropical intraseasonal oscillations. *Proc. Natl. Acad. Sci. USA*, **106**, 8417–8422, doi:10.1073/pnas.0903367106.
- Maloney, E. D., and D. L. Hartmann, 1998: Frictional moisture convergence in a composite life cycle of the Madden–Julian oscillation. *J. Climate*, **11**, 2387–2403, doi:10.1175/1520-0442(1998)011<2387:FMCIAC>2.0.CO;2.
- Mapes, B. E., 2001: Water’s two height scales: The moist adiabat and the radiative troposphere. *Quart. J. Roy. Meteor. Soc.*, **127**, 2353–2366, doi:10.1002/qj.49712757708.
- , P. E. Ciesielski, and R. H. Johnson, 2003: Sampling errors in rawinsonde-array budgets. *J. Atmos. Sci.*, **60**, 2697–2714, doi:10.1175/1520-0469(2003)060<2697:SEIRB>2.0.CO;2.
- , S. Tulich, J. Lin, and P. Zuidema, 2006: The mesoscale convection life cycle: Building block or prototype for large-scale tropical waves? *Dyn. Atmos. Oceans*, **42**, 3–29, doi:10.1016/j.dynatmoce.2006.03.003.
- Matthews, A. J., 2008: Primary and successive events in the Madden–Julian Oscillation. *Quart. J. Roy. Meteor. Soc.*, **134**, 439–453, doi:10.1002/qj.224.
- , D. B. Baranowski, K. J. Heywood, P. J. Flatau, and S. Schmidtke, 2014: The surface diurnal warm layer in the Indian Ocean during DYNAMO. *J. Climate*, **27**, 9101–9122, doi:10.1175/JCLI-D-14-00222.1.
- McNab, A. L., and A. K. Betts, 1978: A mesoscale budget study of cumulus convection. *Mon. Wea. Rev.*, **106**, 1317–1331, doi:10.1175/1520-0493(1978)106<1317:AMBSOC>2.0.CO;2.
- Moncrieff, M. W., D. E. Waliser, M. J. Miller, M. A. Shapiro, G. R. Asrar, and J. Caughey, 2012: Multiscale convective organization and the YOTC virtual global field campaign. *Bull. Amer. Meteor. Soc.*, **93**, 1171–1187, doi:10.1175/BAMS-D-11-00233.1.
- Nitta, T., and S. Esbensen, 1974: Heat and moisture budget analyses using BOMEX data. *Mon. Wea. Rev.*, **102**, 17–28, doi:10.1175/1520-0493(1974)102<0017:HAMBAU>2.0.CO;2.
- Nuss, W. A., and D. W. Titley, 1994: Use of multiquadric interpolation for meteorological objective analysis. *Mon. Wea. Rev.*, **122**, 1611–1631, doi:10.1175/1520-0493(1994)122<1611:UOMIFM>2.0.CO;2.
- O’Brien, J. J., 1970: Alternative solutions to the classical vertical velocity problem. *J. Appl. Meteor.*, **9**, 197–203, doi:10.1175/1520-0450(1970)009<0197:ASTTCV>2.0.CO;2.
- Powell, S. W., and R. A. Houze Jr., 2013: The cloud population and onset of the Madden–Julian oscillation over the Indian Ocean during DYNAMO-AMIE. *J. Geophys. Res. Atmos.*, **118**, 11 979–11 995, doi:10.1002/2013JD020421.
- Praveen Kumar, B., J. Vialard, M. Lengaigne, V. S. N. Murty, and M. J. McPhaden, 2012: TropFlux: Air–sea fluxes for the global tropical oceans—Description and evaluation. *Climate Dyn.*, **38**, 1521–1543, doi:10.1007/s00382-011-1115-0.
- Randall, D. A., Harshvardhan, and D. A. Dazlich, 1991: Diurnal variability of the hydrologic cycle in a general circulation model. *J. Atmos. Sci.*, **48**, 40–62, doi:10.1175/1520-0469(1991)048<0040:DVOTHC>2.0.CO;2.
- Raymond, D. J., 2001: A new model of the Madden–Julian oscillation. *J. Atmos. Sci.*, **58**, 2807–2819, doi:10.1175/1520-0469(2001)058<2807:ANMOTM>2.0.CO;2.
- Redelsperger, J. L., D. B. Parsons, and F. Guichard, 2002: Recovery processes and factors limiting cloud-top height following the arrival of a dry intrusion observed during TOGA COARE. *J. Atmos. Sci.*, **59**, 2438–2457, doi:10.1175/1520-0469(2002)059<2438:RPAFLC>2.0.CO;2.
- Riley, E. M., B. E. Mapes, and S. N. Tulich, 2011: Clouds associated with the Madden–Julian oscillation: A new perspective from *CloudSat*. *J. Atmos. Sci.*, **68**, 3032–3051, doi:10.1175/JAS-D-11-030.1.
- Rowe, A. K., and R. A. Houze Jr., 2014: Microphysical characteristics of MJO convection over the Indian Ocean during DYNAMO. *J. Geophys. Res. Atmos.*, **119**, 2543–2554, doi:10.1002/2013JD020799.
- Rui, H., and B. Wang, 1990: Development characteristics and dynamic structure of tropical intraseasonal convection anomalies. *J. Atmos. Sci.*, **47**, 357–379, doi:10.1175/1520-0469(1990)047<0357:DCADSO>2.0.CO;2.
- Ruppert, J. H., Jr., R. H. Johnson, and A. K. Rowe, 2013: Diurnal circulations and rainfall in Taiwan during SoWMEX/TiMREX (2008). *Mon. Wea. Rev.*, **141**, 3851–3872, doi:10.1175/MWR-D-12-00301.1.
- Sobel, A. H., J. Nilsson, and L. M. Polvani, 2001: The weak temperature gradient approximation and balanced tropical moisture waves. *J. Atmos. Sci.*, **58**, 3650–3665, doi:10.1175/1520-0469(2001)058<3650:TWTGAA>2.0.CO;2.
- , S. Wang, and D. Kim, 2014: Moist static energy budget of the MJO during DYNAMO. *J. Atmos. Sci.*, **71**, 4276–4291, doi:10.1175/JAS-D-14-0052.1.
- Stephens, G. L., P. J. Webster, R. H. Johnson, R. Engelen, and T. L’Ecuyer, 2004: Observational evidence for the mutual regulation of the tropical hydrological cycle and tropical sea surface temperatures. *J. Climate*, **17**, 2213–2224, doi:10.1175/1520-0442(2004)017<2213:OEFTMR>2.0.CO;2.
- Stramma, L., P. Cornillon, R. A. Weller, J. F. Price, and M. G. Briscoe, 1986: Large diurnal sea surface temperature variability: Satellite and in situ measurements. *J. Phys. Oceanogr.*, **16**, 827–837, doi:10.1175/1520-0485(1986)016<0827:LDSSTV>2.0.CO;2.
- Sui, C.-H., K.-M. Lau, Y. N. Takayabu, and D. A. Short, 1997: Diurnal variations in tropical oceanic cumulus convection during TOGA COARE. *J. Atmos. Sci.*, **54**, 639–655, doi:10.1175/1520-0469(1997)054<0639:DVITOC>2.0.CO;2.
- , X. Li, and K.-M. Lau, 1998: Radiative–convective processes in simulated diurnal variations of tropical oceanic convection. *J. Atmos. Sci.*, **55**, 2345–2357, doi:10.1175/1520-0469(1998)055<2345:RCPISD>2.0.CO;2.
- Takemi, T., O. Hirayama, and C. Liu, 2004: Factors responsible for the vertical development of tropical oceanic cumulus convection. *Geophys. Res. Lett.*, **31**, L11109, doi:10.1029/2004GL020225.
- Vialard, J., and Coauthors, 2009: CIRENE: Air–sea interactions in the Seychelles–Chagos thermocline ridge region. *Bull. Amer. Meteor. Soc.*, **90**, 45–61, doi:10.1175/2008BAMS2499.1.
- Virts, K. S., and J. M. Wallace, 2010: Annual, interannual, and intraseasonal variability of tropical tropopause transition layer cirrus. *J. Atmos. Sci.*, **67**, 3097–3112, doi:10.1175/2010JAS3413.1.
- , —, Q. Fu, and T. P. Ackerman, 2010: Tropical tropopause transition layer cirrus as represented by CALIPSO lidar observations. *J. Atmos. Sci.*, **67**, 3113–3129, doi:10.1175/2010JAS3412.1.
- Waite, M. L., and B. Khouider, 2010: The deepening of tropical convection by congestus preconditioning. *J. Atmos. Sci.*, **67**, 2601–2615, doi:10.1175/2010JAS3357.1.
- Waliser, D. E., K. M. Lau, W. Stern, and C. Jones, 2003: Potential predictability of the Madden–Julian oscillation. *Bull. Amer. Meteor. Soc.*, **84**, 33–50, doi:10.1175/BAMS-84-1-33.

- , and Coauthors, 2012: The “Year” of Tropical Convection (May 2008–April 2010): Climate variability and weather highlights. *Bull. Amer. Meteor. Soc.*, **93**, 1189–1218, doi:10.1175/2011BAMS3095.1.
- Webster, P. J., C. A. Clayson, and J. A. Curry, 1996: Clouds, radiation, and the diurnal cycle of sea surface temperature in the tropical western Pacific. *J. Climate*, **9**, 1712–1730, doi:10.1175/1520-0442(1996)009<1712:CRATDC>2.0.CO;2.
- Weckwerth, T. M., J. W. Wilson, and R. M. Wakimoto, 1996: Thermodynamic variability within the convective boundary layer due to horizontal convective rolls. *Mon. Wea. Rev.*, **124**, 769–784, doi:10.1175/1520-0493(1996)124<0769:TVWTCB>2.0.CO;2.
- , T. W. Horst, and J. W. Wilson, 1999: An observational study of the evolution of horizontal convective rolls. *Mon. Wea. Rev.*, **127**, 2160–2179, doi:10.1175/1520-0493(1999)127<2160:AOSOTE>2.0.CO;2.
- Wei, D., A. M. Blyth, and D. J. Raymond, 1998: Buoyancy of convective clouds in TOGA COARE. *J. Atmos. Sci.*, **55**, 3381–3391, doi:10.1175/1520-0469(1998)055<3381:BOCCIT>2.0.CO;2.
- Weller, R. A., and S. P. Anderson, 1996: Surface meteorology and air-sea fluxes in the western equatorial Pacific warm pool during the TOGA Coupled Ocean-Atmosphere Response Experiment. *J. Climate*, **9**, 1959–1990, doi:10.1175/1520-0442(1996)009<1959:SMAASF>2.0.CO;2.
- Wheeler, M. C., and H. H. Hendon, 2004: An all-season real-time multivariate MJO index: Development of an index for monitoring and prediction. *Mon. Wea. Rev.*, **132**, 1917–1932, doi:10.1175/1520-0493(2004)132<1917:AARMMI>2.0.CO;2.
- Wu, Z., 2003: A shallow CISK, deep equilibrium mechanism for the interaction between large-scale convection and large-scale circulations in the tropics. *J. Atmos. Sci.*, **60**, 377–392, doi:10.1175/1520-0469(2003)060<0377:ASCDEM>2.0.CO;2.
- Xu, K.-M., and D. A. Randall, 1995: Impact of interactive radiative transfer on the macroscopic behavior of cumulus ensembles. Part II: Mechanisms for cloud-radiation interactions. *J. Atmos. Sci.*, **52**, 800–817, doi:10.1175/1520-0469(1995)052<0800:IOIRTO>2.0.CO;2.
- Xu, W., and S. A. Rutledge, 2014: Convective characteristics of the Madden–Julian oscillation over the central Indian Ocean observed by shipborne radar during DYNAMO. *J. Atmos. Sci.*, **71**, 2859–2877, doi:10.1175/JAS-D-13-0372.1.
- Yanai, M., and R. H. Johnson, 1993: Impacts of cumulus convection on thermodynamic fields. *The Representation of Cumulus Convection in Numerical Models*, Meteor. Monogr., No. 46, Amer. Meteor. Soc., 39–62.
- , S. Esbensen, and J.-H. Chu, 1973: Determination of bulk properties of tropical cloud clusters from large-scale heat and moisture budgets. *J. Atmos. Sci.*, **30**, 611–627, doi:10.1175/1520-0469(1973)030<0611:DOBPOT>2.0.CO;2.
- Yang, S., and E. A. Smith, 2006: Mechanisms for diurnal variability of global tropical rainfall observed from TRMM. *J. Climate*, **19**, 5190–5226, doi:10.1175/JCLI3883.1.
- Yasunaga, K., M. Fujita, T. Ushiyama, K. Yoneyama, Y. N. Takayabu, and M. Yoshizaki, 2008: Diurnal variations in precipitable water observed by shipborne GPS over the tropical Indian Ocean. *SOLA*, **4**, 97–100, doi:10.2151/sola.2008-025.
- Yoneyama, K., and Coauthors, 2008: MISMO field experiment in the equatorial Indian Ocean. *Bull. Amer. Meteor. Soc.*, **89**, 1889–1903, doi:10.1175/2008BAMS2519.1.
- , C. Zhang, and C. N. Long, 2013: Tracking pulses of the Madden–Julian oscillation. *Bull. Amer. Meteor. Soc.*, **94**, 1871–1891, doi:10.1175/BAMS-D-12-00157.1.
- Zhang, C., 2005: Madden-Julian oscillation. *Rev. Geophys.*, **43**, RG2003, doi:10.1029/2004RG000158.
- , 2013: Madden–Julian oscillation: Bridging weather and climate. *Bull. Amer. Meteor. Soc.*, **94**, 1849–1870, doi:10.1175/BAMS-D-12-00026.1.
- , M. McGauley, and N. Bond, 2004: Shallow meridional circulation in the tropical eastern Pacific. *J. Climate*, **17**, 133–139, doi:10.1175/1520-0442(2004)017<0133:SMCITT>2.0.CO;2.
- , J. Gottschalck, E. D. Maloney, M. W. Moncrieff, F. Vitart, D. E. Waliser, B. Wang, and M. C. Wheeler, 2013: Cracking the MJO nut. *Geophys. Res. Lett.*, **40**, 1223–1230, doi:10.1002/grl.50244.
- Zipser, E. J., 1977: Mesoscale and convective-scale downdrafts as distinct components of squall-line structure. *Mon. Wea. Rev.*, **105**, 1568–1589, doi:10.1175/1520-0493(1977)105<1568:MACDAD>2.0.CO;2.
- Zuluaga, M. D., and R. A. Houze Jr., 2013: Evolution of the population of precipitating convective systems over the equatorial Indian Ocean in active phases of the Madden–Julian oscillation. *J. Atmos. Sci.*, **70**, 2713–2725, doi:10.1175/JAS-D-12-0311.1.